NTNU
Norwegian University of
Science and Technology

Structural and electrochemical characterization of graphite materials for Li ion batteries

Phung Hieu Dinh Tran

Materials Science and Engineering
Submission date: February 2012
Supervisor: Fride Vullum, IMTE
Co-supervisor: Anita Fossdal, SINTEF

Norwegian University of Science and Technology
Department of Materials Science and Engineering

TMT4905 Materials Technology, Master Thesis

AUTUMN 2011

STRUCTURAL CHARACTERIZATION OF GRAPHITE MATERIALS FOR LI-ION BATTERIES

Phung Hieu Dinh Tran

Supervisor: Assoc. Prof. Fride Vullum-Bruer
Co-supervisor: Research Scientist Anita Fossdal (SINTEF)

DEPARTMENT OF MATERIALS SCIENCE AND ENGINEERING

NORWEGIAN UNIVERSITY OF SCIENCE AND TECHNOLOGY

My utmost gratitude to
Sri Srimad Chaitanya Candra Prabhu,
who was the main motivation for completing this thesis

Table of Contents

1 Summary

1.1 English

The purpose of this study is to find a correlation between the crystallite sizes in the basal plane direction of graphite materials, used in carbon anodes in Lithium-ion batteries. Carbon anodes are the most common type of anode used in rechargeable Lithium-ion batteries today. The two major causes of capacity fading in graphite anodes is structural disordering during cycling and SEI (solid electrolyte interface) formation, which causes a loss of active graphite material and loss of active lithium-ion respectively.

On this basis, the crystallite size in the basal plane direction L_a of graphite are measured by structural characterization methods for later comparison with the performance of the graphite powder when used as a carbon anode. In this work, three characterization methods have been utilized to characterize four different types of graphite powders. These three characterization methods are Raman spectroscopy, X-ray powder diffraction and SEM analysis, with special emphasis on Raman spectroscopy due to its flexibility when it comes to sample preparation methods. Three different sample preparation methods have been carried out on the graphite powders before doing Raman measurements.

A comparison of the results from the Raman measurements shows a clear trend in which the calculated R-ratio is dependent on the sample preparation method, where the R-ratio is largest for samples prepared as carbon anodes. It is very likely that this trend is attributed to the increase in R-ratio due to mechanical milling of the graphite powders as a part of the processing steps of the carbon anode sample.

Determining the L_a value with X-ray powder diffraction is usually a difficult task due to poor resolution of the diffraction peaks necessary to derive the L_a value. This is due to preferred orientation of non-spherical shaped graphite powders when the powder is applied directly on a Si-sample holder for X-ray diffraction measurements. However, by air spraying the graphite powders mixed with ethanol, the particle are more random oriented, giving visible diffraction peaks needed to derive the L_a value.

It has been shown that Raman spectroscopy is an unreliable method for determining the L_a value by comparing the results from X-ray with the results from Raman measurements. However, if Raman spectroscopic measurements are used together with X-ray measurements, a new linear relationship between the X-ray measured L_a value and the Raman R-ratio can be derived.

1.2 Norsk

Hensikten med denne studien er å finne en sammenheng mellom krystallitt størrelsen i basal planets retning i grafitt materialer som brukes i karbon anoder i Lithium-ione batterier. Karbon anoder er den vanligste typen av anoder som brukes i oppladbare Lithium-ione batterier i dag. De to viktigste årsakene til kapasitet tap i grafitt anoder er strukturelle forandringer under syklus og SEI (Solid Electrolyte Interface) formasjon, noe som fører til tap av aktiv grafitt materiale og tap av aktiv litium ioner henholdsvis. På denne bakgrunn er krystallitt størrelsen i basal planets retning L_a av grafitt målt ved strukturelle karakteriserings metoder for senere sammenligning med resultatene av grafitt pulver når det brukes som en karbon anode.

Tre karakteriserings metoder har blitt benyttet i denne oppaven for å karakterisere fire ulike typer grafitt pulver. Disse tre karakteriserings metodene er Raman-spektroskopi, X-ray pulver diffraksjon og SEM analyse, med særlig vekt på Raman spektroskopi på grunn av metodens fleksibilitet når det gjelder prøvepreparerings metoder.

Tre forskjellige prøvepreparerings metoder har blitt utført på grafitt pulver før Raman målinger ble foretatt. En sammenligning av resultatene fra de utførte Raman målingene viser en klar tendens der beregnet R-ratio er avhengig av prøvepreparerings metoden, hvor R-ratio er størst for prøver forberedt som karbon anoder. Det er svært sannsynlig at denne trenden kan tilskrives økningen i R-ratio på grunn av mekanisk sliping av grafitt pulver som en del av de forskjellige prosesserings trinnene av karbon anode prøven.

Utledning av L_a verdien med røntgendiffraksjon er vanligvis en vanskelig oppgave på grunn av dårlig oppløsning av diffraksjon toppene nødvendig for å utlede L_a verdien. Dette skyldes foretrukket orientering av ikke-sfærisk formede grafitt pulver når pulveret påføres direkte på en Si-prøve holder for røntgendiffraksjons målinger. Men ved spray lakkering av grafitt pulver blandet med etanol, vil grafitt partiklene være mer tilfeldig orientert, noe som gir synlige diffraksjons topper som trengs for å utlede L_a verdien.

Det er påvist at Raman spektroskopi er en upålitelig metode for bestemmelse av L_a verdien gjennom sammenligning av resultatene fra røntgendiffraksjons målingene med resultatene fra Raman målingene. Likevel kan en ny lineær sammenheng mellom X-ray L_a verdi og Raman R-ratio utledes hvis Raman spektroskopiske målinger brukes sammen med røntgendiffraksjons målinger.

2 Introduction

2.1 Lithium Batteries - a Promising Technology

The rechargeable lithium-ion battery is the most common type of rechargeable battery used in portable electronics today, ranging from mp3 players, laptops, shavers, and it has also found its way into the HEV (Hybrid Electric Vehicle) market. The most common type of rechargeable lithium-ion battery is the C/$LiCoO_2$ cell, which was first commercialized by Sony Energytech in Japan in 1991. Ever since its commercialization, the lithium-ion battery sales has experienced a steady growth and been the dominating type of rechargeable battery for portable electronics, Figure 2.1 [34, 47].

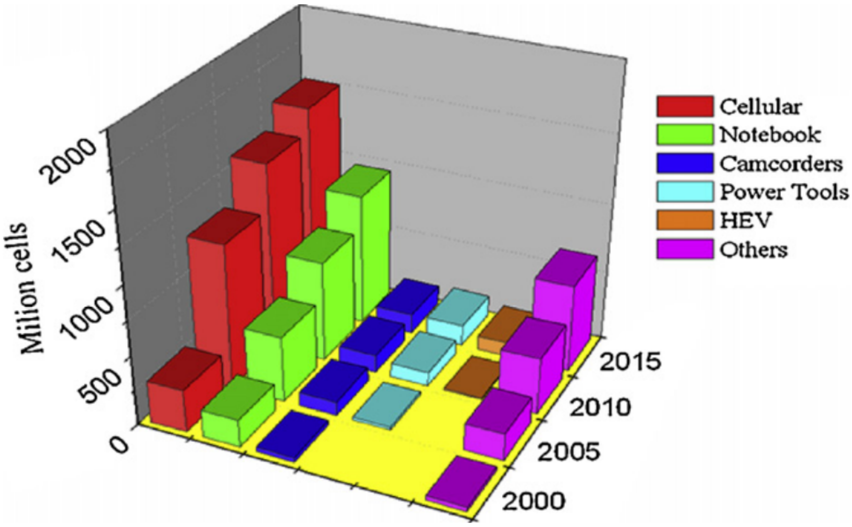

Figure 2.1: Evolution of the lithium-ion battery sale in the consumer market [47, p. 2420]

The main motivation behind the utilization of lithium-ion batteries in electronic portables and HEVs is shown in Figure 2.2 which compares the gravimetric and volumetric densities of different types of rechargeable batteries. From the figure, it can be seen that lithium-ion batteries exhibits excellent volumetric [Whl^{-1}] and gravimetric [$Whkg^{-1}$] energy densities. This result implies that batteries based on lithium can deliver more electrical energy per weight and per volume than non-lithium based batteries. For this reason, it is widely used in portable consumer electronics such as laptops, mobile phones, mp3 players, etc.

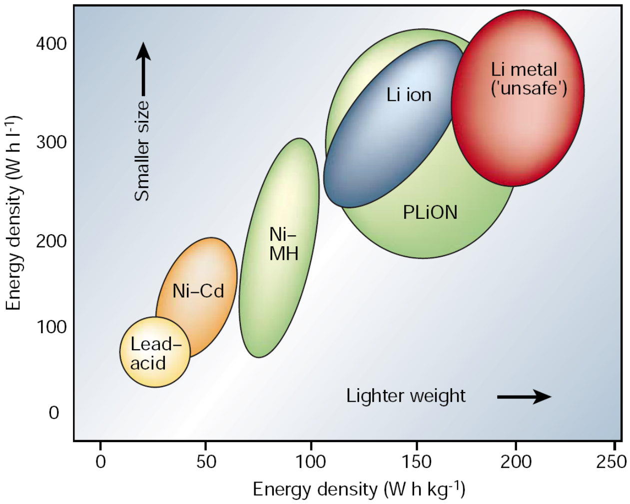

Figure 2.2: Comparison of different types of rechargeable batteries [52, p. 359]

However, as it is with all technologies, the lithium-ion technology also has a few shortcomings. One of the major shortcomings is the difficulty in implementing this technology on larger scales project due to overheating problems, which make safety guarantee a challenge. Examples are the recalling of 22,000 laptop batteries by dell in 2006 and 100,000 laptop batteries by Sony in 2008 due to overheating problems [31,56].

Nonetheless, the lithium-ion technology remains a promising technology for the future due to emerging research on nanomaterials in lithium-ion rechargeable batteries [35]. This can be asserted by the electric bicycle, called Killacycle, which are powered by lithium iron nano-phosphate ($LiFePO_4$ as cathodes) battery cells manufactured by A123 Systems [8]. This electric bicycle has the capability to reach a remarkable speed of 60 mph in 0.97 seconds [6]. In addition, this nanophosphate battery technology has excellent abuse properties [8].

2.2 Background

The main focus of this thesis is structural characterization methods of graphite materials used in rechargeable lithium ion batteries as anodes. The characterization methods used to analyze the material were SEM (Scanning Electron Microscopy) analysis, Raman spectroscopy and X-ray powder diffraction.

The emphasis has been on measuring the L_a value (the graphite crystallite size in the basal direction) by Raman spectroscopy, with X-ray powder diffraction and SEM analysis as supporting characterization techniques. Special emphasis is put on Raman spectroscopic measurements due to the versatility of measuring Raman scattered laser light from a sample. This implies that samples needs little or no sample preparation for Raman measurements, giving the possibility of detecting structural changes of a material which has been tested without having to do any sample preparation of the tested material.

The two major causes of capacity fade of Li-ion batteries which are contributed by graphite anodes is structural disordering during cycling and SEI (solid electrolyte interface) formation, which causes a loss of active graphite material and loss of lithium-ion respectively [35]. On this basis, the L_a value are measured to find out if there is any relationship between this value and the max capacity, the capacity loss (which might be due to structural disorder), the rate capability and the SEI formation.

3 Theory

This chapter consists of 5 main sections. The first section presents the general theory about lithium-ion batteries, with emphasis on carbon anodes. The second section deals mainly with the general theory behind Raman spectroscopy, in which the theory is based upon four books [24,36,45,48] and two review articles [12,22] which present the theory behind Raman spectroscopy. The third section consists of an introduction on the characteristic of the Raman spectroscopy of graphite where the theory is based upon three review articles [12, 18, 44]. In the fourth section, a short introduction on the X-ray powder diffraction technique is explained [61] and how to determine the L_a value from X-ray diffraction patterns are explained [28]. The theory behind SEM analysis is omitted due to the relative simple characterization method used in the SEM studies.

3.1 Lithium-ion Batteries

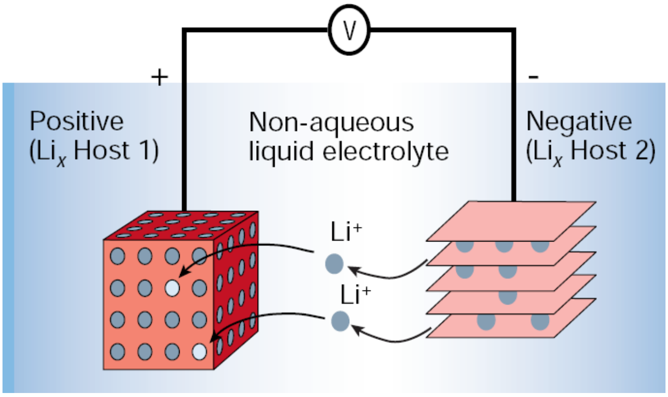

Figure 3.1: Schematic illustration of Li^+-ion transportation from the anode to the cathode during discharge [52, p. 360]

Batteries can be divided into two categories; *primary batteries*, which are not rechargeable and *secondary batteries*, which are rechargeable. The most common types of secondary batteries today are the lead-acid, nickel-cadmium, nickel-metal-hydride and lithium-ion rechargeable battery. In terms of energy density, secondary lithium-ion batteries are superior (Figure 2.2).

A basic lithium-ion secondary battery consist of two electrodes, an anode and a cathode separated by an electrolyte solution which contains dissociated salts, which comes in different configurations, Figure 3.2.

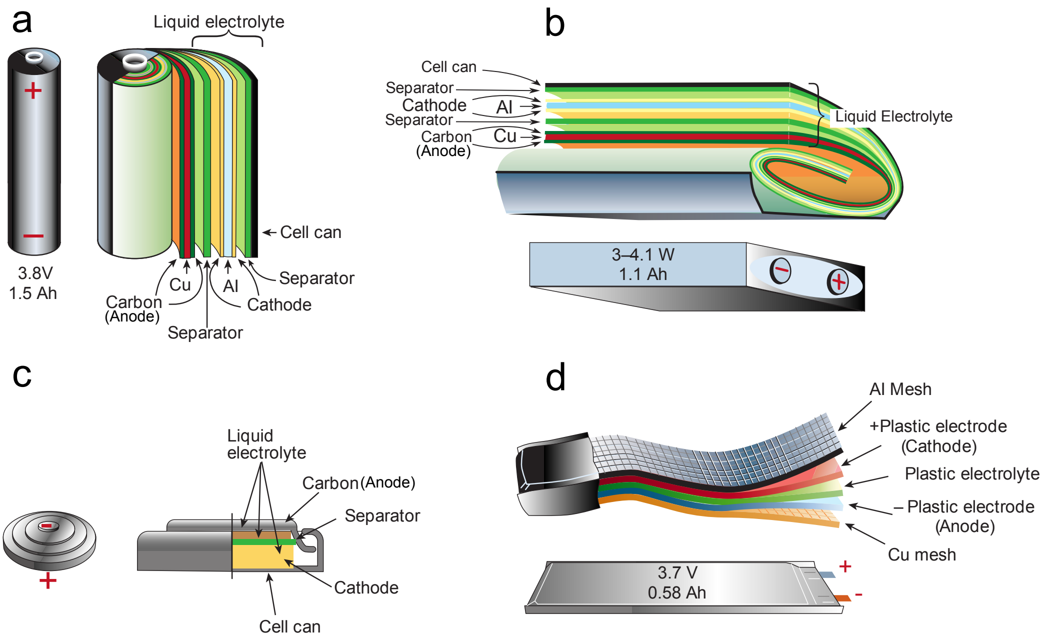

Figure 3.2: Schematic illustration showing the shape and components of various Lithium-ion battery configurations: **(a)** Cylindrical **(b)** Prismatic **(c)** Coin (or button) **(d)** Thin and flat [52, p. 361]

The electrolyte solution enables Li^+ to be reversibly transferred between the two electrodes. The reversible process of Li^+ transportation between the two electrodes involves intercalation/deintercalation into/from the electrodes. These types of electrodes works as a host matrix, usually called lithium intercalation compounds. During discharge, the Li^+-ions are extracted (de-interclated) from the anode (usually graphite) and inserted (intercalated) into the cathode, Figure 3.1), whereas the opposite process occurs during charging.

3.1.1 Secondary Lithium-ion Batteries

During discharge, oxidation occurs at the anode, whereas a reduction occurs at the cathode. Since $LiCoO_2$ was the first cathode material commercially used (and the most common type), chemical reaction formulas showing the redox reaction between a $LiCoO_2$ cathode and a Li_xC_6 anode are used in this context to show the reactions which governs during discharge of a lithium-ion battery:

Anode half-reaction: $Li_xC_6 \rightarrow xLi^+ + xe^- + 6C$

Cathode half-reaction: $Li_{1-x}CoO_2 + xLi^+ + xe^- \rightarrow LiCoO_2$

Overall reaction: $Li_xC_6 + Li_{1-x}CoO_2 \rightarrow LiCoO_2 + 6C_6$

During charging, the half-reactions and the overall reaction goes from right to left instead.

3.1.2 Critical Parameters

Open Circuit Voltage

The open-circuit voltage V_{oc} is expressed by the difference in the lithium chemical potential between the cathode and the anode:

$$V_{oc} = \frac{\mu_c - \mu_a}{F} \tag{3.1}$$

where μ_c is the chemical potential of the cathode, μ_a is the chemical potential of the anode, and F is the Faraday constant. The open-circuit voltage V_{oc} is dependent on the energies involved in both the electron transfer and the Li^+ transfer. The magnitude of the open-circuit voltage V_{oc} is however limited when thermodynamic stability is taken into consideration. In order to inhibit unwanted reduction or oxidation of the electrolyte, the difference in the chemical potential between the cathode and the anode must be smaller than the band gap E_g:

$$eV_{oc} = \mu_c - \mu_a < E_g \tag{3.2}$$

where e is the magnitude of the electron charge [40].

Capacity

The capacity of a secondary lithium-ion battery is a measure of the battery's ability to store electrical charge, which is measured in ampere hours (Ah). Approximation of the capacity for a battery is expressed by Peukert's Law [23].

$$C = It \tag{3.3}$$

where C is the capacity when discharged at a rate of 1A. I is the current drawn from the battery and t is the amount of time (in hours) that a battery can sustain. In order to have a high capacity, the electrode materials should have a high volumetric and gravimetric energy density, which would imply a high number of available charge carriers per volume and per mass unit of the material.

Cycle Life

Cycle life is the number of cycles (one charge/discharge) a battery can sustain before failure. The capacity of a battery decreases with the number of cycles performed on the battery. A battery is considered no longer usable when the capacity has decreased to 80%-60% of its original capacity before cycling. Lithium-ion batteries with carbon anodes exhibit a notable *irreversible capacity loss* after the first cycle due to SEI (Solid Electrolyte Interface) formation and co intercalation processes at the anode [40].

Charge/Discharge Rate

The charge/discharge rate is usually expressed as the C-rate. If a battery has a capacity of 1000 mAh, it would provide a current of 1000 mA for one hour if discharged at 1C. A discharge rate at 1C would therefore draw a current equal to the capacity of the battery, whereas a battery discharged at a rate of C/2 would provide a current of 500 mA for two hours [15].

Rate Capability

The rate capability of a battery is its ability to deliver current. Batteries with a high rate capability are able to deliver a lot of current whereas batteries with a low rate capability are only able to deliver small currents. In addition, batteries with a high rate capability can tolerate a high charging current, while batteries with a low rate capability has a low tolerance against high charging currents.

3.1.3 Graphitic Carbon Anodes

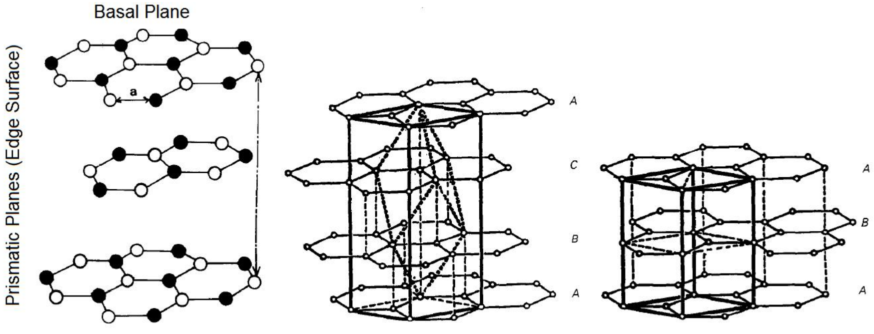

(a) (b) (c)

Figure 3.3: (a) Illustration of the graphite structure and its basal plane (b) Illustration showing the ABC-type (c) Illustration showing the ABAB-type [17, p. 987-988]

The graphite structure consist of layers of carbons arranged in a "honeycomb-like" network, usually called graphene sheets, Figure 3.3a. These sheets are "stacked" on each other in a repeating manner. Bonding of the graphene sheets are due to weak Van der Waals forces. These sheets are also referred to as the basal planes in the graphite structure. The prismatic edge or edge plane, are also shown in the figure. If a graphite powder is very crystalline, it is possible to distinguish the basal planes and the edge planes in a SEM (Scanning Electron Microscope), Figure 3.4. The edge planes are shown as stripes on the surface of a powder particle.

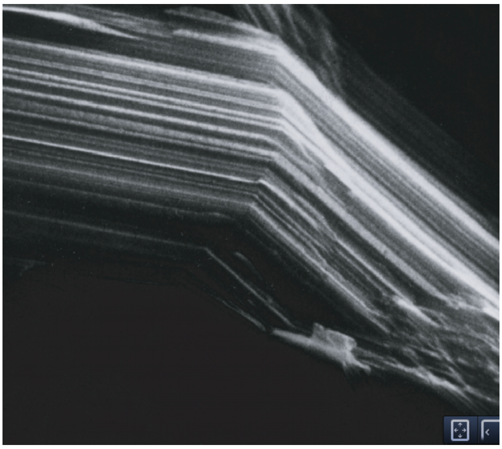

Figure 3.4: SEM micrograph showing the clearly visible edge planes of very crystalline TIMREX graphite powder particle from Timcal company [4, p. 1]

There are two different types of graphite, dependent on the manner the graphene sheets are stacked, either AB stacking (hexagonal) or the less common ABC stacking (Figure 3.3b and c). In reality, perfectly stacked graphite crystals are not readily available due to small energy transformation between the AB and ABC stacking. During intercalation of the graphite anode, Li-ions enters into the structure via the prismatic planes of the graphite structure. The Li-ions is therefore situated in-between the graphene sheets after intercalation. During de-intercalation, the reverse process occurs, Li-ions are de-intercalated out of the honey-comb layers [40].

The L_a Value

The L_a value is the crystallite size in the basal direction in the graphite structure, Figure 3.5). This value can be determined by using a well established procedure where X-ray diffraction measurements are used [28].

Irreversible Capacity Loss

During the first cycle of a coin cell which contains a carbon anode, a notable loss of capacity occurs, which is frequently referred to as the irreversible capacity loss (ICL). When the battery is charged for the first time, there is a decrease in capacity during

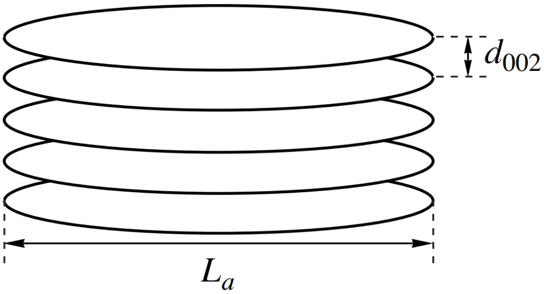

Figure 3.5: Illustration showing the L_a in the basal plane direction of a graphite crystallite. The circular discs represent layers of graphene sheets [14, p. 929]

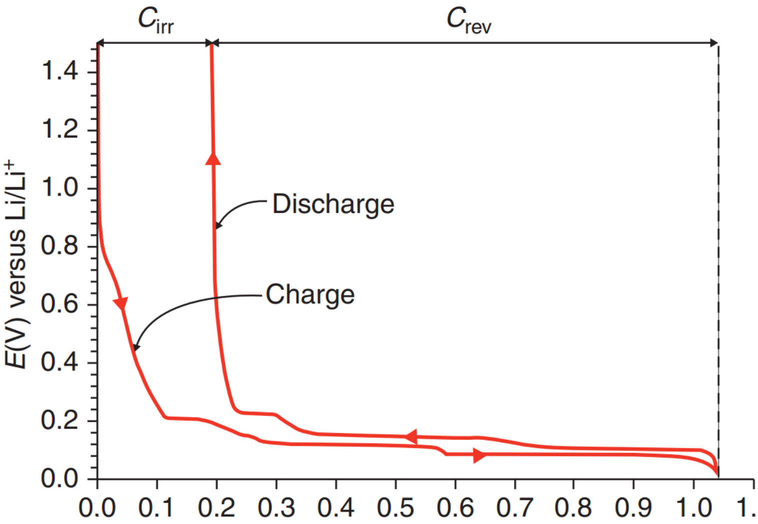

Figure 3.6: First charge/discharge curve showing the irreversible capacity loss. Also shown in the Figure is how the magnitude of irreversible capacity (C_{irr}) are measured and how the reversible capacity (C_{rev}) are measured [34, p. 16]

the first discharge. This notable loss of capacity after the first discharge is the ICL of the battery, Figure 3.6. Only about 80-95% of the first charge is retained after the first discharge. The capacity which has been lost is referred to as the irreversible capacity, abbreviated as C_{irr}, whereas the retained capacity, or reversible capacity is abbreviated as C_{rev}. The ICL occurs due to reactions of Li-ions with the graphite anode during lithiation of carbon. In addition, the lithiated carbon also reacts with the electrolyte, which governs most of the ICL [41, 62]. This reaction between the electrolyte and the carbon anode forms a layer on the carbon anode, usually called a Solid Electrolyte Interface (SEI).

Solid Electrolyte Interface

The formation of a protective film, frequently called the Solid Electrolyte Interface (SEI) takes place mainly in the first cycle of a secondary battery. This layer forms by reduction of the carbon anode surface during the first intercalation (first charge of the battery) of Li-ions into the carbon anode host: $xLi^+ + xe^- + 6C \rightarrow Li_xC_6$

This SEI-layer protects the anode by passivation which protects the carbon anode from further considerable degradation due to reduction of the carbon anode. The SEI-layer also acts like a sieve, being selectively permeable to Li-ions, but impermeable to any other electrolyte component that would react with Li-ions [57]. Thickness and resistance of the film has been shown to increase during charge and discharge. Increase of the thickness and resistance of the SEI, which would lead to higher over potentials and electronic insulation of the carbon anode are considered to be one of the main reasons for capacity fading during cycling [49].

3.2 Raman Spectroscopy

Raman spectroscopy is named after the Indian physicist C. V. Raman who discovered the Raman effect together with K. S. Krishnan in 1928 [39]. The Raman effect is the inelastic scattering of an incident photon on a molecule (Raman scattering) due to interaction with the vibrational modes of that molecule.

Since the vibrational modes operate in discrete energy levels and is characteristic for each molecule, the energy of the scattered photon is dependent on the molecule in which the incident photon has interacted with. Therefore, the scattered photon can be measured by an instrument which can give a Raman spectrum as an output, acting as a "fingerprint" for a each molecule. The consequence is that Raman spectroscopy is able to provide unique structural information from all types of compounds due to a molecules unique vibrational modes.

One major advantage in Raman spectroscopy is that it needs little sample preparation since it uses laser light to induce the so called Raman effect (or Raman scattering) to occur in the sample, which are detected by the Raman instrument. Samples can therefore be solid, liquid or gas, and sample polishing is usually not a requirement.

An another advantage is that these measurement can be done in normal atmosphere in room temperature since the sample only need to be irradiated with laser light. The laser also has an advantage of being able to penetrate glass, leading to the fact that Raman measurements can be done on volatile liquids which are sealed inside glass containers.

However, an obvious limitation of using laser light is that it is restricted to the sample surface only if the sample is solid due to the laser not being able to penetrate the sample. As a result, Raman scattering from the sample are restricted to the sample surfaces which have been irradiated with laser.

3.2.1 Electromagnetic Radiation

All types of lights (including IR light) are in the category of electromagnetic radiation. Electromagnetic radiation behaves as waves and consists of an electric field component and a magnetic field component, which oscillates in a sinusoidal behavior normal to each other, Figure 3.7. The Raman effect is the result of the interaction of the electric field component and the dipole moment of a molecule, therefore, only the electric field component will be relevant for topics about Raman spectroscopy.

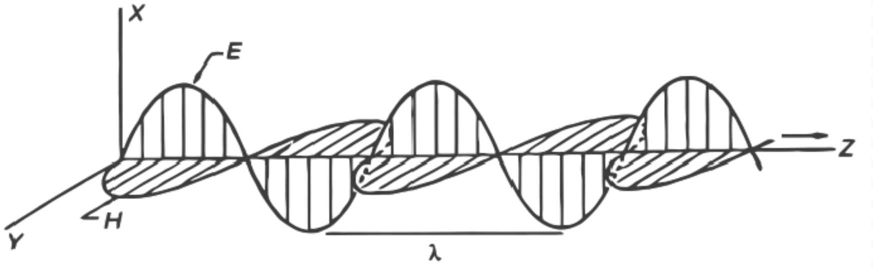

Figure 3.7: The electric field component E and the magnetic field component H oscillates normal to each other. The wavelength λ is the distance between two crests [24, p. 3]

The wavenumber, $\tilde{\nu}$, which is the number of waves per unit length (cm$^-1$) is given by:

$$\tilde{\nu} = \frac{\nu}{c/n} = \frac{1}{\lambda}\ [\mathrm{cm}^{-1}] \tag{3.4}$$

where ν is the frequency (number of cycles per time), c is the speed of light, n is the refractive index the wave is passing through and λ is the wavelength. Furthermore, according to quantum theory, the photon is a quantum of electromagnetic radiation, where the energy of a photon is denoted as E_p:

$$E_p = h\nu = hc\tilde{\nu}\ [\mathrm{J}] \tag{3.5}$$

where h is the Planck's constant. From Equation 3.5, it becomes apparent that the energy of a photon is proportional to the frequency ν, or the wavenumber $\tilde{\nu}$.

3.2.2 Vibrational Modes

The Raman effect occurs when photons induces a change of the dipole moment of a molecule, leading to a change in the vibrational mode of the molecule. Therefore, in order to obtain a basic understanding of the Raman effect, it is important to have some knowledge about the theory behind the different vibrational modes of a molecule.

A molecule vibrates with a certain frequency, and the number of vibrational modes (or normal modes of vibration) vary according to the number of atoms a molecule consists of. For a linear molecule, the number of vibrational modes is 3N - 5, where N is the number of atoms the molecule consists of. For non-linear molecules, the number of vibrational modes is 3N - 6. This would mean that for a diatomic atom such as H_2, the number of vibrational modes would simply be 3(2) - 5 = 1, which is simply stretching of the bonds, as shown in Figure 3.8a.

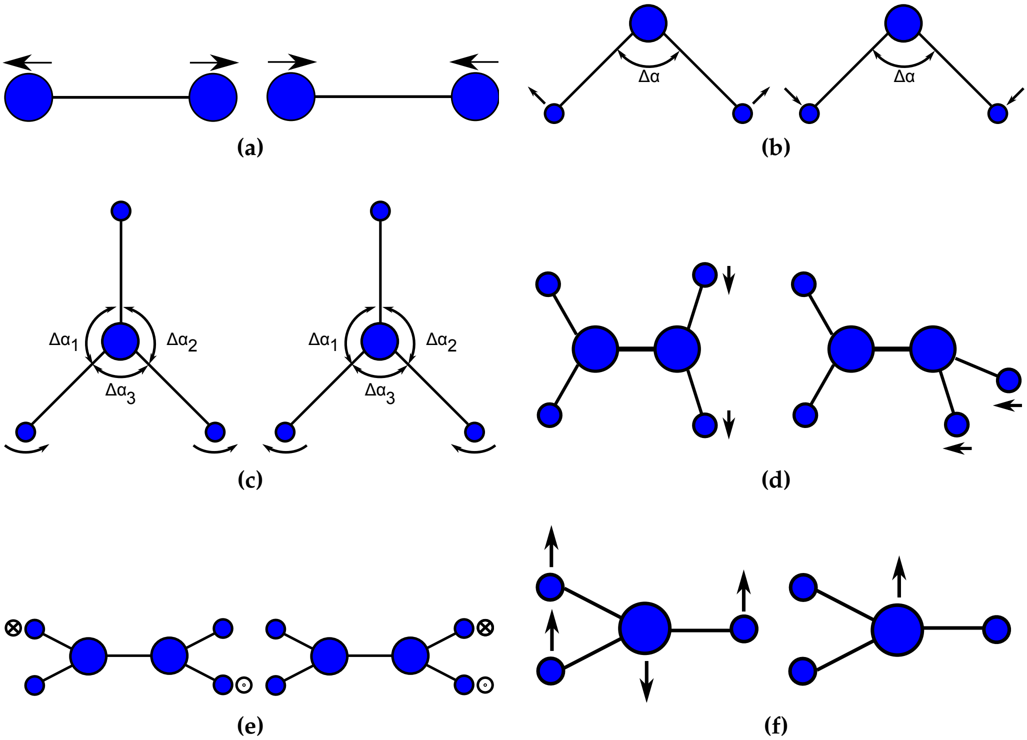

Figure 3.8: Vibrational modes: **(a)** Stretching mode **(b)** Angle deformation mode **(c)** Rocking mode **(d)** Wagging mode **(e)** Twisting mode (⊗ denotes an arrow which points into the paper plane, whereas ⊙ denotes an arrow which point out of the paper plane) (f) Out of plane deformation mode (Redrawn from Narayana [45, p. 24-28])

For molecules other than diatomic molecule, there can be more than one vibrational mode (see Figure 3.8), such as:

- stretching (stretching and contraction of the bonds between atoms)
- angle deformation (change in the bonding angle)
- rocking (e.g. two atoms moves as a whole in the same plane in a pendulum like motion relative to the rest of the molecule)
- wagging (e.g. two atoms moves as a whole side by side in a pendulum like motion relative to the rest of the molecule)

- twisting (twisting of the molecule through a center of rotation)
- out of plane deformation (e.g. one atom moves back and forth in the opposite phase as the other atoms in the molecule)

In addition, each vibrational mode vibrates in a specific frequency which depends on atomic mass (molecular components), force constants (bonding strength), symmetry of the molecule, strain, etc. Explanation of the vibrational mode dependent frequencies is briefly explained in the next section.

3.2.3 The Simple Stretching Mode of a Diatomic Molecule

As mentioned before, a molecules vibrational modes operate in discrete energy levels, similar to discrete electronic energy levels for electrons in an isolated atom. These discontinuous vibrational energy levels give rise to characteristic bands in a Raman spectrum. In order to understand how the vibrational modes of a molecule interact with a photon, the simple vibrational mode of a diatomic molecule is considered herein.

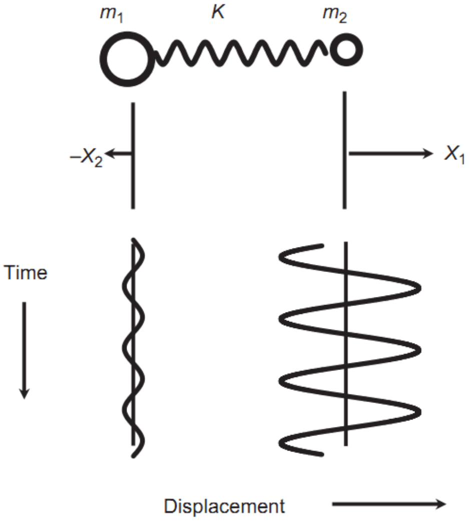

Figure 3.9: K is the spring constant, m_1 and m_2 are the masses of the two atoms and X_1 and X_2 is the displacement. [36, p. 10]

The simple stretching mode of a diatomic molecule behaves as a simple quantum harmonic oscillator. Figure 3.9 above shows a simple quantum mechanical harmonic oscillator with two different masses; mass m_1 and mass m_2. The spring is mass less and the displacement of the masses from the equilibrium position is denoted X_1 and X_2 which represents two different atoms in a diatomic molecule, where K is the spring constant. As evident from the figure, the displacement varies sinusoidal with time.

Both masses oscillate with the same frequency and goes through their equilibrium positions simultaneously. The center of mass of the whole system is stationary and the amplitudes is inversely proportional with the masses respectively:

$$-\frac{X_1}{X_2} = \frac{m_2}{m_1} \tag{3.6}$$

Furthermore, the following expression for wavenumber $\tilde{\nu}$ applies for the simple harmonic system above:

$$\tilde{\nu} = \frac{1}{2\pi c}\sqrt{K(\frac{1}{m_1} + \frac{1}{m_2})}\ [\mathrm{cm}^{-1}] \tag{3.7}$$

As evident from the expression above, the wavenumber is dependent on the force constant and the masses. The force constant is proportional to the strength of the chemical bond. Consequently, a triple bond has a stronger force constant than a double- or a single bond.

3.2.4 Vibrational Energy Level Diagrams

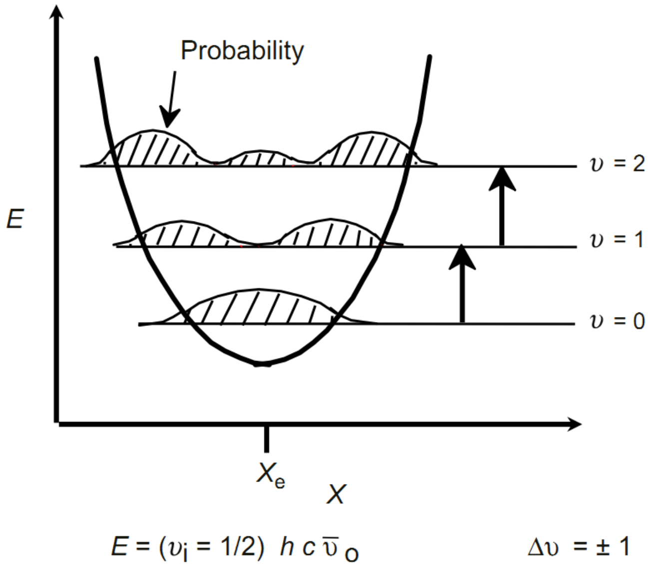

Figure 3.10: Plot showing the parabolic relationship between the potential energy (E on the y-axis) and the displacement X. The potential energy is at its minimum at the equilibrium distance X_e [36, p. 12]

The potential energy PE of a diatomic molecule is given by:

$$PE = \frac{1}{2}KX^2 \tag{3.8}$$

In Figure 3.10, the parabolic relationship between the potential energy PE and the distance X between the two atoms are shown. At the equilibrium distance X_e, the potential energy is at its minimum value. However, the vibrational energy derived from equation 3.8 is not continuous, rather, it is quantized. Consequently, a molecule can only have certain vibrational energy states, which is similar to electrons which can only have certain energy states in isolated atoms. In addition, a molecule can go from one vibrational energy state to another which is also similar to electrons jumping from one energy state to another by excitation.

Following expression for the different energy levels applies for the harmonic system:

$$E_i = (v_i + \frac{1}{2})h\nu \quad v_i = 0, 1, 2... \tag{3.9}$$

where ν is the vibration frequency and v_i is a quantum number which can only have integer values, Figure(3.10). For harmonic systems, v can only change by an increment of ± 1, which is called a fundamental transition. Other transitions such as $v = 1$ to $v = 3$ or $v = 0$ to $v = 2$ is not allowed. At ground state where $v = 0$, the energy is referred to as the zero point energy ($E = 1/2 hv$). This zero point energy cannot be removed from the molecule.

Although the harmonic oscillation model of a diatomic molecule gives the simplest picture of the stretching vibrational mode, it is rather unrealistic. When the displacement increases towards the distance equivalent to dissociation of the molecule, the deviation from harmonic behavior increases, as shown in Figure 3.11 below. Also shown in the figure is the dissociation energy D_o, which is larger than the spectroscopic energy

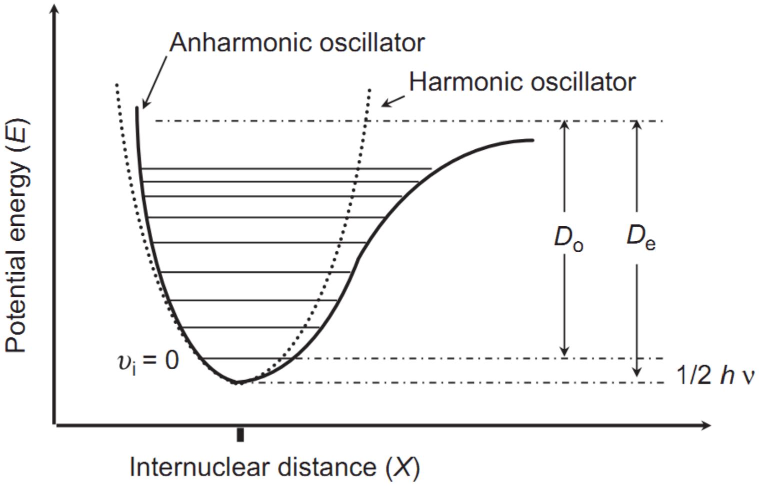

Figure 3.11: Plot comparing the harmonic system (dotted line) with the anharmonic system (full line) [36, p. 13]

.

D_e (the energy required to dissociate the molecule if the molecule was at the minimum of the potential energy plot). As mentioned before, the zero point energy at $v = 0$ cannot be removed from the molecule, for this reason, the actual dissociation energy of the molecule D_o is lower than D_e. The result is a simple expression of D_o, given by

$$D_o = D_e - (\frac{1}{2})hv \tag{3.10}$$

In anharmonic system, transitions involving larger transitions are allowed. Transitions which gives a change of $v = \pm 2$ is called the first overtone, whereas a change of $v = \pm 3$ is called the second overtone, and so on. Most molecules would be in the ground state ($v = 0$), as a result, most transition would originate from this ground state (see next section). There is less probability for transitions larger than the fundamental transitions to occur, as a consequence, these types of transition is of weaker intensity.

3.2.5 The Raman Scattering Process

Molecules have a certain dipole moment, which is determined by its charge distribution. This charge distribution is determined by the electron cloud. When a molecule is exposed to electromagnetic radiation (here: monochromatic light), the electric field component interacts with the oscillating dipoles with a certain dipole moment. Scattering occurs when the electric field component has successfully perturbed a change in a molecules polarizability (the tendency for a charge distribution to be distorted by an electric field), hence its dipole moment is changed.

The dipole moment is given by

$$\mu = \alpha E \tag{3.11}$$

where μ is the induced dipole moment, α is the polarizability and E is the electric field. There must be a variation in the polarizability induced by a molecular vibration in order for scattering to occur. The explanation above is the classical explanation of the Raman scattering process.

However, it is also preferable to know the theory behind Raman scattering in terms of quantum mechanics. The three different scattering processes is illustrated in Figure 3.12a. Only the Stokes Raman- and Anti-stokes Raman scattering is relevant since these two scattering processes is a result of a change in the dipole moment. For Rayleigh scattering, there is no change in dipole moment after scattering, hence, no change in vibrational state has occurred after interaction. In order for a photon to be absorbed, the energy of the incident photon has to be equal to the energy difference between two states.

Absorption leads to an excitation from a vibrational state to a virtual state (non-existent state), see Figure 3.12a. This excitation process may occur either from the ground state or from the vibrational state. However, there is a higher probability for excitation to occur from the ground state. The absorption is followed by a relaxation

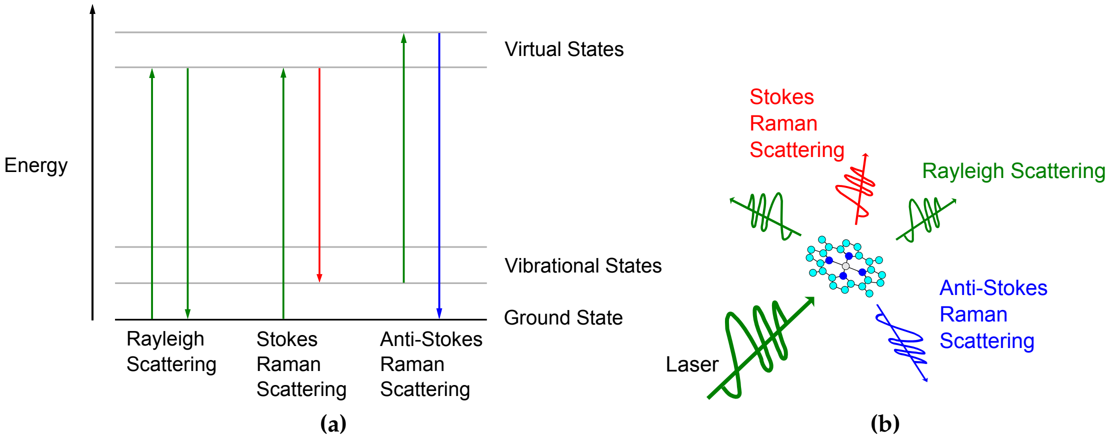

Figure 3.12: Schematic explanation of the three different scattering processes: **(a)** Schematic energy level diagram illustrating the different scattering processes. The excitation energy is represented with the green upward arrows (note: all the upward arrows has the same length, which represent the "mono" excitation energy of monochromatic light in a Raman experiment). In Rayleigh scattering, the energy of the scattered photon (green downward arrow) has the same energy as the incident photon. In Stokes Raman scattering, the scattered photon has a lower energy than the incident photon , whereas in Anti-stokes Raman scattering, the scattered photon has a higher energy than the scattered photon [9]. **(b)** Analogy of the scattered light explained by the energy diagram, showing the scattering of laser light (shown as green) into Rayleigh scattered light (green), Stokes Raman scattered light (red) and anti-Stokes Raman scattered light (blue) [5, p. 1].

from the virtual state to the vibrational state where a new photon is created and scattered.

If the relaxation energy equals the energy of the incident photon, the scattered photon will have the same energy as the incident photon. This type of scattering is called elastic Rayleigh scattering since there is no change in energy. If the relaxation energy is smaller than the excitation energy, the energy of the scattered photon will be smaller than the incident photon. This is called inelastic Stokes Raman scattering where a transference of energy from the incident photon to the molecule has occurred (hence a scattered photon with lower energy). Consequently, the molecule has a different vibrational energy after scattering.

The opposite process of the Stokes Raman scattering is the Anti-stokes Raman scattering. In this process, excitation occurs from a higher vibrational state than the ground state followed by relaxation to the ground state. In the Anti-stokes Raman scattering process, an energy transference from the molecule to the photon occurs instead, leading to the scattered photon having a higher energy than the incident photon.

3.2.6 Raman Spectrum

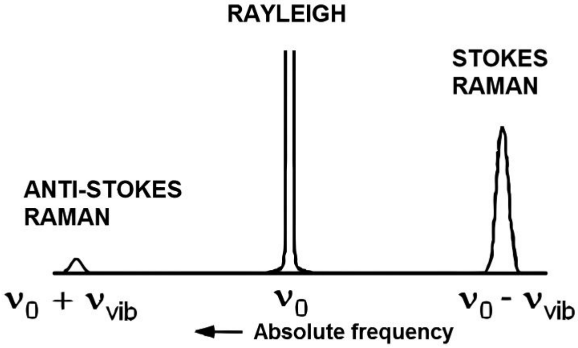

Figure 3.13: Schematic Raman plot showing where the Rayleigh, Anti-Stokes Raman and the Stokes Raman peaks occur. ν_0 is the excitation frequency whereas ν_{vib} is the molecular vibration of the molecule [12, p. 1280].

A plot of the intensity of the scattered Raman radiation versus frequency difference is called a Raman plot (see Figure 3.13). The frequency difference is commonly referred to as the Raman shift, usually denoted in cm^{-1} which is the unit of wavenumber $\tilde{\nu}$. Since the Raman shift is a difference value, it is independent of the frequency of the incident radiation.

The Stokes Raman intensity lines has a higher intensity than the Anti-stokes Raman lines since most molecules are in the vibrational ground state. Consequently, Raman spectra are plotted as intensity versus the Stokes shifted frequencies. The Raman shift of the Raman intensities depends on the vibrational modes of the molecules in the radiated sample. As a result, the Raman shift is characteristic for each molecule since each molecule has different vibrational modes (briefly explained in section 3.2.2, 3.2.3 and 3.2.4),

3.2.7 Confocal Raman Microscopy

A confocal Raman microscope can be regarded as a light microscope (optical microscope) with inbuilt equipments which can measure the Raman scattering of a sample (see Figure 3.14). The laser light is focused on the sample through the microscope objective, leading to Raman scattering of the laser light from the sample. The Raman scattered laser light is refocused through the pinhole aperture which acts like a spatial filter. This scattered Raman signal is received by the spectrometer where it is dispersed (distributed) on the CCD (charged couple device) camera which produces a Raman spectrum.

b

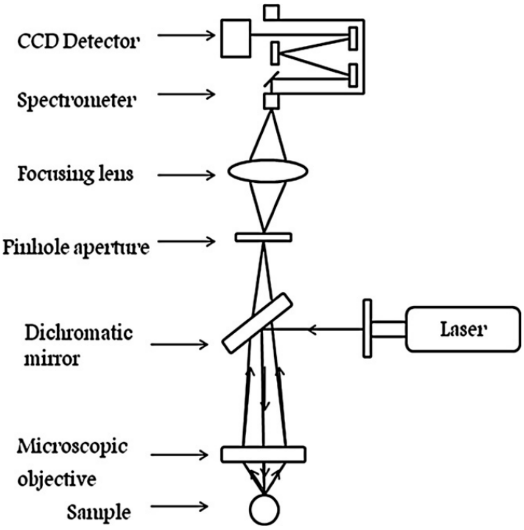

Figure 3.14: Schematic illustration of a confocal Raman microscope

3.3 Raman Spectroscopy of Graphite

Raman Active Modes

It has been observed that graphite has two Raman active vibrational modes, which is referred to as the E_{2g_1} mode and the E_{2g_2} mode. The E_{2g_2} mode has been observed as a peak in perfectly crystalline carbon materials at around 1582 cm^{-1} which is inherent in all carbon materials. This E_{2g_2} mode has also appeared as a peak at around 3248 cm^{-1} and is referred to as an overtone of the E_{2g_2} mode. The E_{2g_1} mode is less known and has been theoretically been estimated to appear at 210 cm^{-1} as a peak.

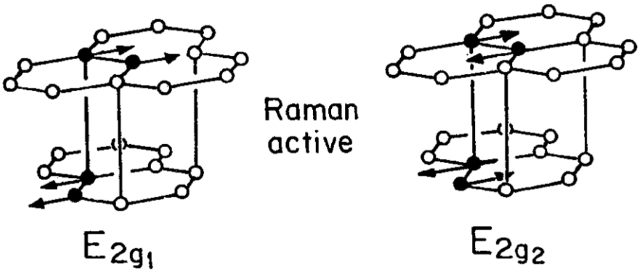

Figure 3.15: The two Raman active vibrational modes in graphite [18, p. 1481]

Raman Spectrum of Graphite

The Raman spectrum of graphite is divided into a first order region between 1100 and 1800 cm^{-1} and a second order region between 2200 and 3400 cm^{-1} (after Tuinstra and Koenig [55, 59]). Only the first order region is considered herein since only the first order region has been studied in this work. Generally, the first order region consist of a characteristic peak for carbon materials at 1̃582 cm^{-1} which is referred to as the G peak in the literature. This G peak is due to the E_{2g_2} Raman active mode mentioned above, Figure 3.16. The G peak is inherent in all carbon materials and this peak is the only peak visible in the first order region for perfectly crystalline carbon materials.

In multicrystalline carbon materials, another peak in the first order region appears in the first order region at 1355 cm^{-1} which is referred to as the D peak (frequently referred to as the disorder induced peak in the literature). Another peak, referred to as the D′ peak at 1620 cm^{-1} can be observed in less crystalline materials. These peaks have been attributed to a mechanism called double resonance scattering (see next section).

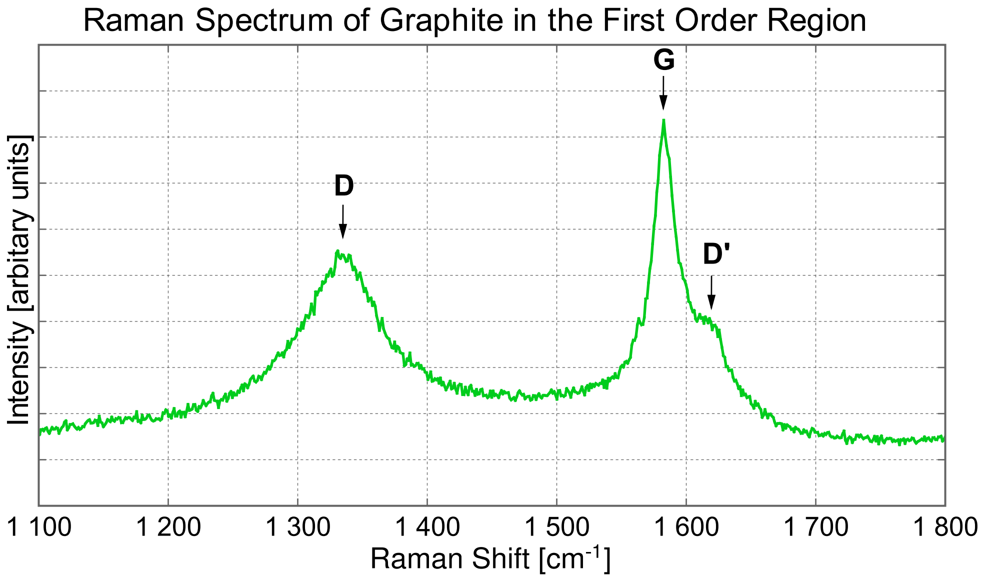

Figure 3.16: The graphite spectrum of the first order region showing the D-peak, the G peak and the D′ peak

3.3.1 Double Resonant Scattering

According to the theory about Raman scattering, the band position is apparently independent of the energy of the electromagnetic radiation. This implies that the band position is fixed regardless of the magnitude of the laser excitation frequency. However, published literatures since the pioneering work of Raman on graphite in 1970 by Tuinstra and Koenig has shown that the frequency of the D- and D′ band shifts to higher energies (lower Raman shift values) with increasing excitation energy.

In addition, the shift has been shown to be linear over a wide range of excitation energies [37, 43, 54, 58, 60]. It was later proven almost two decades later that this process occurs due to a double resonant phonon scattering by Thomsen et. al (A thorough explanation of this subject matter is not included due to the complexity of this mechanism) [53].

3.3.2 Determination of the L_a Value by Raman Spectroscopy

Correlation between the L_a value and the ratio of the peak intensities of the D peak and the G peak were founded in the work published by Tuinstra et al. [55] in 1970. The measured L_a value by x-ray diffraction of the graphite crystallites and the ratio between the D and G peak had a remarkable empirical correlation, Figure 3.17a.

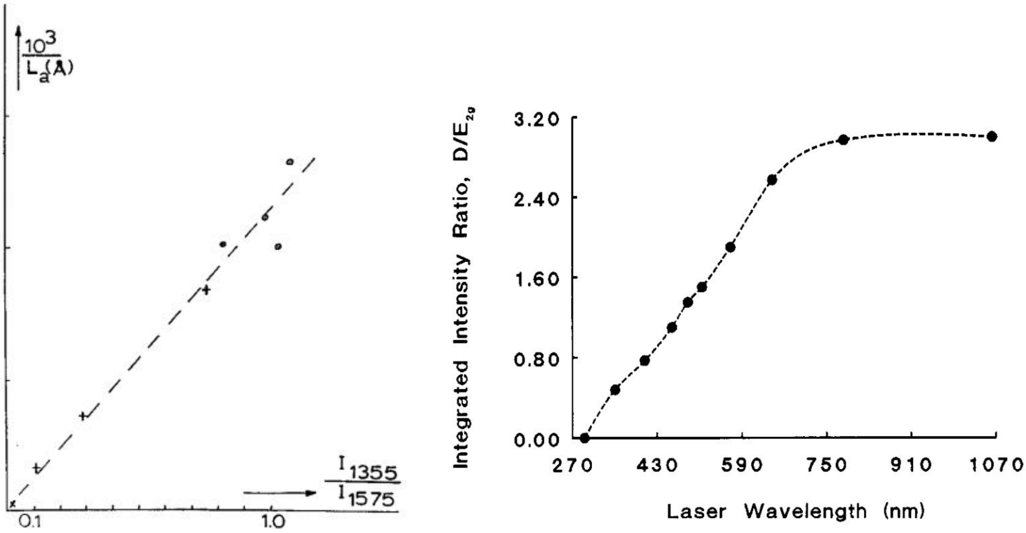

(a) **(b)**

Figure 3.17: (a) Correlation between x-ray measured *La* and the ratio *R* (after Tuinstra et al. [55]). **(b)** The intensity ratio R as a function of laser excitation frequency, after the work of Wang et al. [60] where all the samples were polished GC-20.

An empirical relationship between the L_a value and the ratio between the D-peak and the G-peak intensities (called the R-ratio) were later developed by least square regression by Knight et. al, the relationship were based on the results by Tuinstra et al.

and other literatures [33,43], given by

$$L_a = \frac{4.4}{R}[nm], \text{ where } R = \frac{I_D}{I_G} \tag{3.12}$$

where I_D is the D-peak intensity and I_G is the G-peak intensity. However, this empirical relationship was based upon a laser excitation frequency of 488 nm. This implies that equation 3.12 is empirically valid only for laser with a laser excitation frequency of 488 nm (as mentioned above) since later published literature has shown that the R value also varies with the laser excitation frequency [16,38,54,60] (see Figure 3.17b).

In addition, calculation of the R-ratio is somewhat ambiguous in the literature where some authors calculate the R-ratio from the peak height intensity of the I_D band and the I_G band. Others have used the integrated peak intensity of the two bands instead [63]. In this work, a He-Ne laser with an excitation frequency of 632.8 nm is used, equation 3.12 will therefore have to be modified. This have been adapted by Goers et al. [25], where a correction factor f_L was empirically derived from the work of Wang et al. (Figure 3.17b) [60], given by:

$$f_L = \frac{R(632.8nm)}{R(488nm)} \tag{3.13}$$

For the 632.8 nm laser, the correction factor f_L equals 2.2. The final modification of Equation 3.12 is then given by:

$$L_a = \frac{4.4}{R} f_L[nm] \tag{3.14}$$

It is important to note that the correction factor of 2.2 is derived from the result of glassy carbon samples where the R value is calculated from integrated intensities (not from peak height intensity) of D- and G-peaks, see Figure 3.17b. S

ince the equation above is empirically derived, variations from this equation are expected. Later published literatures still shows a roughly linear relationship between L_a and R, where R is inversely proportional to the L_a value [26,27,30,42]. However, Nikiel et al. has reported a larger deviation from the relationship in Equation 3.12 on their study on nuclear grade graphites, Figure 3.18a [42].

There is however a clear deviation from the inverse proportional relationship when the crystallite size gets below a certain size at around 2nm [16, 63]. There are also other factors which affect the R-ratio which are proven by published literatures since the pioneering work of Tuinstra et al. One of the factors which modify the R-ratio is whether the Raman measurements are done on the basal planes of the graphite powders or the edge planes of the graphite powders. The trend is that the calculated R-ratio is higher when the measured Raman results are obtained from graphite edge planes, compared to when the measured Raman results are obtained from the graphite basal planes [19,32,51].

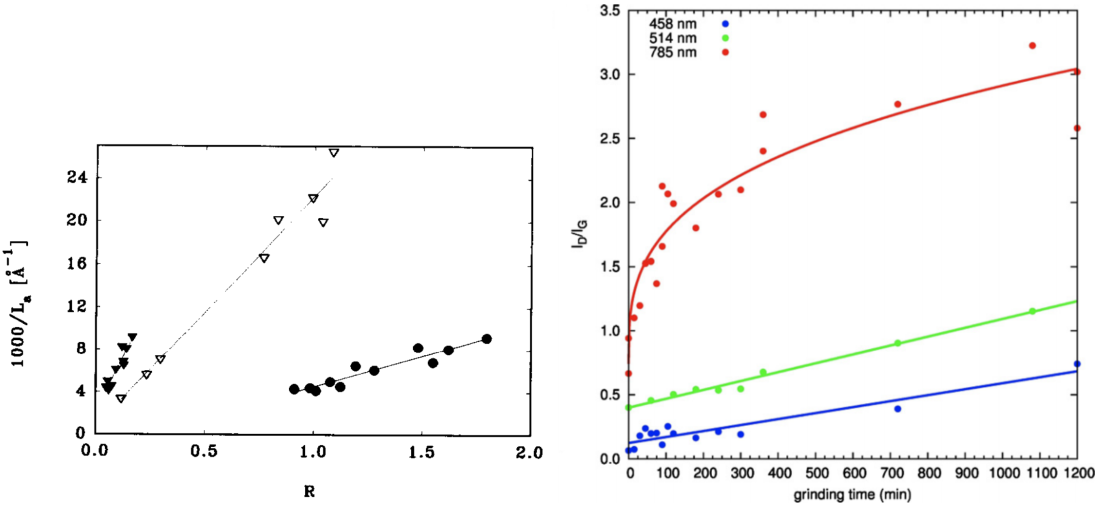

(a) **(b)**

Figure 3.18: **(a)** Deviation from the relationship in Equation 3.12. ▽ shows the relationship from Tuinstra et al. in which Equation 3.12 has been derived. • shows the relationship from nuclear graphites which was found in the work by Nikiel et al. **(b)** The relationship between R-ratio and grinding time. The magnitude of the R-ratio increases much faster when the laser excitation frequency is lower [54, p. 222]

An another factor which affects the R-ratio is mechanical grinding of the carbon powder. Tommasini et al. have shown that the R-ratio are affected by grinding in a study where grinding was done on nanographites before Raman measurements (see Figure 3.18b [54]. The trend is that the magnitude of the R-ratio is proportional with the ball milling time, where the magnitude of the R-ratio increases much faster when the laser excitation frequency is lower (higher wavelength). Although the R-ratio is such a sensitive parameter, several authors of published literatures on Raman spectroscopic study on graphite have relied on the relationship between the X-ray measured L_a value and the R-ratio alone, using Raman measurements of graphite to determine the L_a value [50, 63].

The motivation behind using Raman measurements alone is due to that the powder diffraction patterns of graphite often show poor resolution of the diffracted intensity peaks which originates from the 110 reflection needed to calculate the L_a value (see section 3.4.4 [13, 50]. However, Cuesta et al. have shown that large discrepancies between the measured L_a value from x-ray and the ratio of the peak intensities of the D peak and the G peak might occur [20].

3.4 X-ray Diffraction

3.4.1 Basic Principles

X-rays are electromagnetic radiation with wavelength at approximately 1 Å(10^{-10}). Generation of X-rays occur when highly charged particles such as electrons are accelerated through 30 000 V before colliding with matter. For instance, when highly charged electrons collide with Cu metal, Cu metal become ionized as a result of the accelerated electrons knocking out a electron in the 1s orbital of the Cu atom, Figure 3.19a. Consequently, an electron from the outer orbitals, either from 2p or from 3p relaxes to the vacant 1s level to occupy it. The energy which is released during the transition is emitted as X-ray radiation. X-ray radiation coming from a transition from 2p to 1s is called $K\alpha$ whereas x-ray radiation coming from a transition from 3p to 1s called $K\beta$. The transition $K\alpha$ and $K\beta$ is always fixed, which is always 1.5418 Åand 1.3922 Åfor Cu. The result is a characteristic x-ray emission spectrum of Cu, showing the $K\alpha$ and $K\beta$ as peaks occurring at those wavelengths mentioned, Figure 3.19b. The $K\alpha$ is used in x-ray diffraction experiments since this radiation has a stronger intensity than the $K\beta$ radiation.

Also shown in Figure 3.19b is a $K\alpha_1$ and a $K\alpha_2$. This is due to the two possible spin states of electrons occupying the 2p level, which implies that $K\alpha_1$ and $K\alpha_2$ comes from the transitions of two electrons from the 2p level with opposite spins. In the x-ray spectra shown in Figure 3.19b is also something called white radiation. This radiation is due to electrons which are accelerated are slowed down or stopped by the collision. The electrons lose some energy which is converted into electromagnetic

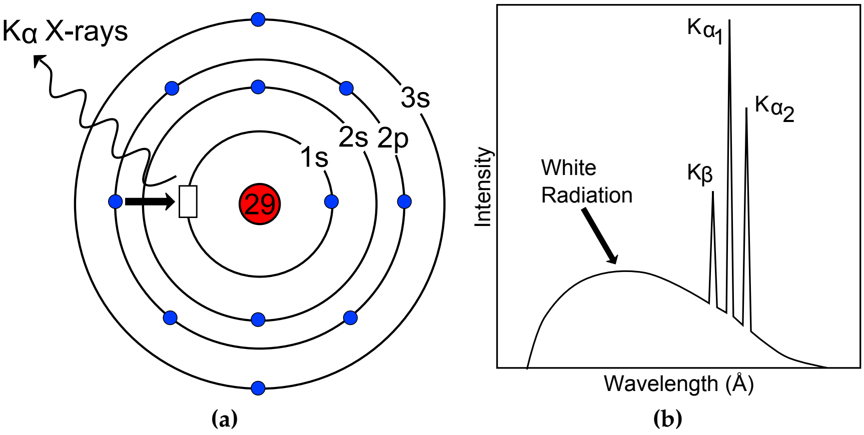

(a) (b)

Figure 3.19: (a) Schematic diagram showing how X-rays are generated in Cu. An electron from the 1s shell is ionized, leading to an electron from the 2p subshell to fall into the empty 1s level. **(b)** X-ray emission spectrum of Cu (redrawn from West [61, p. 128]

radiation. The sharp monochromatic peaks which are discussed above is characteristic for each element, consequently, the Kα and Kβ radiation occurs at different wavelength for different elements. These monochromatic radiations are generated when electrons are accelerated with a voltage >10 000V before colliding with matter.

X-ray Tube

An x-ray tube, Figure 3.20 ,is an electron tube under vacuum which generates x-rays by accelerating electrons through a high voltage, causing the electrons to collide against a target (here:Cu) with high velocity. The tungsten filament, which acts as a cathode supplies electrons to the Cu anode trough a high voltage in the range of 30 000 V to 100 000 V [11]. The tube has to be under vacuum to prevent oxidation of the tungsten filament. X-ray radiation from the target leaves the tube through Be (beryllium) windows due to low atomic number. This is due to x-rays being able to pass through materials with low atomic weight (which makes Be a good fit with an atomic number of 4) but are stopped by materials with high atomic weight such as lead. Continuous cooling of the anode to prevent melting is necessary since most of the energy from the incident electrons are converted to heat, only a small fraction is converted into x-rays.

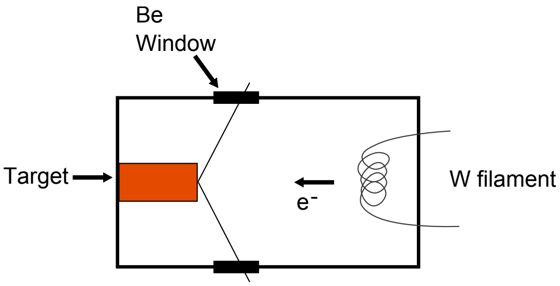

Figure 3.20: A schematic drawing of an X-ray tube (redrawn from West [61, p. 129]

Monochromatic x-ray radiation is used in most diffraction experiments. Since Kα is most intense in the x-ray spectrum of a material, all other wavelengths are filtered out. Consequently, the white and the Kβ has to be filtered out. For instance, Ni filter are used for Cu radiation since Ni has a Kα radiation (1.488 Å) which lies between the values of Kα and Kβ in Cu. All radiation from Cu which is higher than 1.448 Åhas sufficient energy (including the K$beta$) to ionize the Ni filter. In other words, the Ni filter absorbs those radiation from Cu which has a wavelength smaller than 1.448 Åso that only a small fraction of white radiation and a clean monochromatic Kα are left after passing through the Ni filter.

3.4.2 Bragg's Law

We will here consider the Bragg approach to get a basic understanding on how x-ray beams are diffracted from a sample made up of powders. This approach regards crystals having layers or planes which are regarded as semi-transparent mirrors. Some of the X-rays are reflected from the planes with a reflection angle equal to the incident angle. The rest of the x-ray are transmitted to be subsequently reflected by succeeding planes. Figure 3.21 shows how Bragg's law is derived. Two adjacent incident x-ray beams, beam 1 and beam 2 are reflected from planes A and B. The reflected beams are beam 1′ and beam 2′. Constructive interference occurs when beam 1′ and beam 2′ are in phase, which means that the extra distance beam 22′ has to travel relative to beam 11′ must equal a whole number of wavelengths.The distance between plane A and B is d, usually referred to as the d-spacing and the angle between the incident beam and the plane is θ, called the Bragg angle. The relation between the d-spacing and the Bragg angle are related with the distance xy, given by

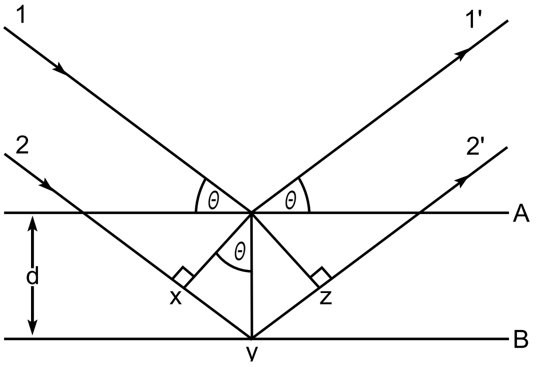

Figure 3.21: Sketch showing the derivation of Bragg's law (redrawn from West [61, p. 134]

$$xy = yz = d \sin\theta$$

where

$$xyz = 2d \sin\theta$$

and

$$xyz = n\lambda$$

as a result,

$$2d \sin\theta = n\lambda \tag{3.15}$$

Equation 3.15 is the celebrated Bragg's law. This law is only applicable at conditions where there are constructive interference, which implies that the reflected beams are in phase.

When the incident angle is different than the Bragg angle, the reflected beams are out of phase, destructive interference occurs which leads to cancellation of the reflected beams.

Bragg's law puts strict restrictions on when reflection occurs. The incident angle has to stay within a few tenths of degree of the Bragg angle in order for the validity of Bragg's law. If not, cancellation (destructive interference) will occur instead. These mirror like planes which are considered in Bragg's law are the set of planes which can be derived from the crystals structures. In the theory of crystallography, crystals consist of atoms arranged in a 3D pattern, or grid, which can be divided into set of planes in various orientation. For simple crystal structures, the planes might correspond to layers of atoms. However, this doesn't apply for more complex crystal structures. Therefore, it is important to note that the semi mirror lake planes in crystals are not always layers consisting of atoms.

In addition, some of the assumptions which are made in Bragg's law might be obscure. One of the reason is that diffraction is due to the interaction of x-rays with atoms, not due to the atomic spacing. An another reason is that the atoms does not reflect X-rays but scatter or diffract them in all directions. However, the derivation of Bragg's law where crystals consist of semi transparent like mirror gives the same result as a rigorous mathematical treatment instead.

3.4.3 X-ray Powder Diffraction

A simple schematic of an X-ray powder diffractometer are shown in Figure 3.22. The X-ray powder diffractometer consist of an X-ray tube, acting as a source of X-ray radiation (usually monochromatic). When the x-ray radiation hits the sample, the X-rays are diffracted at various angles which are detected by a detector. The diffraction angles are thereby recorded, which gives an X-ray diffraction pattern where the diffraction angles are recorded as high intensity peaks compared to the rest of the diffraction pattern. This is due to that constructive interference occurs at the diffraction angle (or the Bragg angle) whereas destructive interference occurs otherwise (see section 3.4.2).

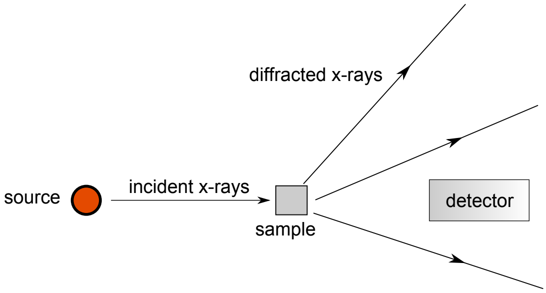

Figure 3.22: A schematic sketch of a X-ray diffractometer (redrawn from West [61, p. 135]

Ideally, the finely powder sample should have crystals which are randomly oriented, which would give lattice planes randomly oriented in every possible orientation. For all the crystals present in the powder sample, an ideal case is that at least some lattice planes are oriented at the Bragg angle, θ, which results in diffraction. The powder sample is scanned with a constant angular velocity relative to the angle between the incident beam and the sample surface. When diffraction occurs at a certain angle, the detector detects the high intensity diffracted beams, showing as high intensity peaks in the diffraction pattern at this Bragg angle. The result is a diffraction pattern which shows diffraction peaks as high intensity lines at various Bragg angles, Figure 3.23. These high intensity peaks are "reflection" at a certain Bragg angle from various set of planes, such as 110, 100, 111 etc.

If the X-rays generated from the X-ray tube does not pass through a monochromator (which filters out Kα_2 radiation, leaving only the Kα_1 to pass through), then two high intensity peaks appears next to each other within a narrow angle span, these two peaks are reflection for one set of planes, originating from two different wavelengths. One peak has a much larger intensity than the other, coming from the Kα_1 whereas the peak with lower intensity is from the Kα_2 radiation. The goal is to always obtain a powder sample which contains random crystal arrangement. The opposite case is something called *preferred orientation* which can give errors into the measured intensities.

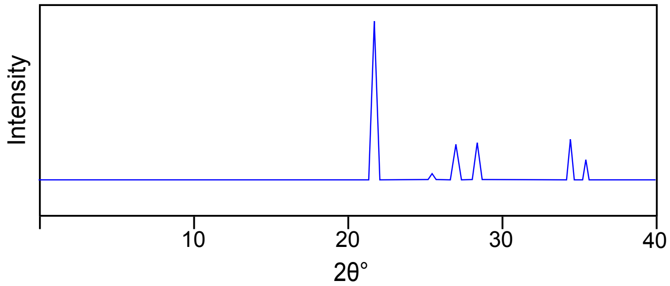

Figure 3.23: A schematic sketch of an x-ray diffraction pattern showing the high intensity as a function of 2θ (2θ is the double of the Bragg angle θ which are more commonly used in X-ray diffraction patterns) (redrawn from West [61, p. 139]

Preferred orientation occurs when materials crystallize in non-spherical way. For instance, clays usually crystallize into cubes and some cubic materials crystallize into cubes and which breaks up into smaller cubes upon crushing. These types of materials tend to sit on their faces in a powder aggregate which results in a non-random average orientation.

Two mains factors determine the diffraction pattern; size and shape of the unit cell and the atomic number and position in the cell. As a result, the diffraction pattern of a sample acts like a fingerprint. Many crystalline materials have the same crystal structure (rock salt, fluorite, spinel, etc.), but the dimensions of the unit cell are different in size and the atoms in the unit cell is different, thus, the scattering patterns are different for each material. For instance, KF, KCl and KI have the rock salt structure but their diffraction patterns are different due to the reasons mentioned.

3.4.4 Determination of the L_a Value by X-ray Powder Diffraction

In this work, the method applied for measuring the L_a value are based upon the well established method published by Iwashita et al. [28]. Only a short excerpt a presented herein with no derivations since the focus have been mainly on the magnitude of the L_a value. Figure 3.24a shows a typical X-ray scan between 75 ° to 80 ° 2θ for a mixture of carbon and silicon powder (10-20wt% silicon according to the crystallinity of the carbon powder). The metal used in the X-ray tube for generating x-rays is Cu. The value

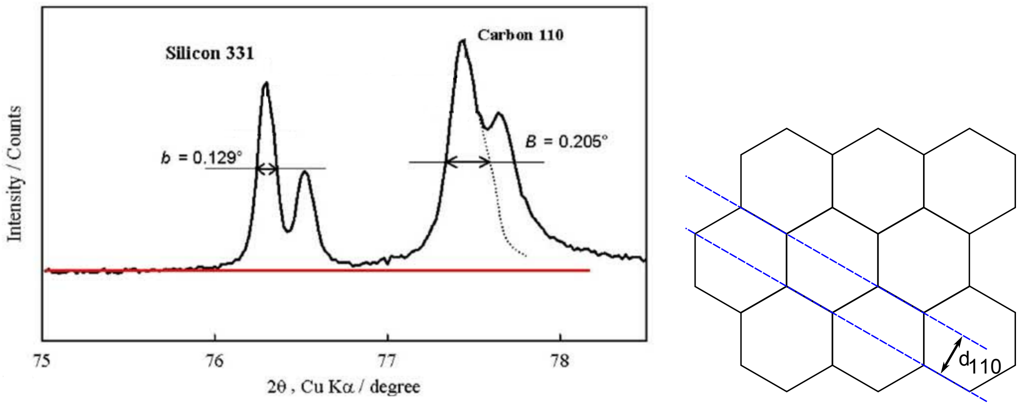

(a)

(b)

Figure 3.24: (a) Sketch showing how the b and B value are measured [28, p. 711]. **(b)** Schematic drawing showing how the 110 planes are oriented relative to the graphite structure [3, p. 2]

b is the FWHM of the diffracted $K\alpha_1$ from the 331 reflection of silicon at 76.305 ° and the B is the FWHM of the diffracted $K\alpha_1$ from the 110 reflection of carbon at 77.434 °. $K\alpha_2$ peaks from the 331 reflection of silicon and 110 of carbon at 76.523 ° and 77.668 ° are either filtered away by a monochromater or stripped away by an X-ray diffraction analysis software. The 110 carbon correspond to set of planes which are perpendicular to the basal planes of graphite, Figure 3.24b The L_a value in graphite calculated from x-ray diffraction are given by

$$L_a = \frac{1.13}{\beta}[nm] \tag{3.16}$$

where

$$\beta = B(0.9981266 - 0.0681532v - 2.592769v^2 + 2.621163v^3 - 0,9584715v^4$$

and

$$v = \frac{b}{B}$$

4 Experimental

The samples were prepared from four different graphite powders. Two of them are received from the company Timcal, called Timrex SFG44 and Timrex SLP30 which are commercially available. The SLP30 type is usually used as an intercalation agent in carbon anodes whereas SFG44 is usually used as an conductive additive [7]. The other two types of graphite powders are received from the company Elkem, called Elkem 57 and Elkem 58. These two materials are not commercially available and are supplied as samples for investigations.

The size distribution of the four different graphite powders are summarized in Table 4.1.

	Particle Size Distribution [μm]		
Sample	D10	D50	D90
SFG44	7.70	23.80	48.80
SLP30	8.00	16.00	32.00
Elkem 57	N/A	16.40	35.12
Elkem 58	N/A	16.03	34.7

Table 4.1: Particle size distribution for the four different graphite powders: The definition of D10 is that 10 mass % of the powder has powder particles with a diameter lower than this value and 90 mass% has a diameter larger than this value. Similarly, D90 means that 90 mass% of the powder has particle diameters lower than this value, etc.

4.1 Raman Spectroscopic Studies

4.1.1 Sample Preparation for Raman Measurements

Three different sample preparation methods were carried out for the graphite powders. Carbon casted on copper, graphite pellets and graphite mixed with isopropanol for drying. The reason behind making three different samples is to confirm that the results from the Raman spectroscopic measurements are independent of the sample preparation methods. Before sample preparation, the graphite powders were dried at 120 °C under vacuum overnight before use.

Carbon casted on copper

This sample preparation method is the procedure for making carbon anodes for testing in CR2016[1] coin cells. The purpose behind this sample preparation method is to see if there are any trends in structural changes of a carbon anode before and after cycling inside a coin cell. A slurry is first made, consisting of Graphite, Carbon Black (CB) PVDF (Polyvinylidene Fluoride) dissolved in NMP (N-Methyl-2-pyrrolidone). The carbon black used was Super P obtained from the company Timcal, PVDF is from the company Kynar and the NMP is provided by Sigma Aldrich.

The weight ratio between the three ingredients were 40:1:3.2 of Graphite, CB and PVDF. PVDF were first dissolved in NMP under magnetic stirring in a beaker, thereafter CB and Graphite were added to the NMP mix. Total weight of slurry was 40 g.

The slurry was thereafter ball milled with a planetary ball miller (Retsch PM100) for 20 min with 5 Al_2O_3 balls (ϕ=30 mm) in a 500 mL grinding jar at 150 RPM. To remove bubbles, the slurry was then transferred to an Erlenmeyer flask to be stirred under vacuum for 2 hours at the lowest stirring speed before casting.

Casting was done on Cu-foil on a tape caster (K Control Coater from RK Print Coat Instruments) using a grooved rod with a casting thickness at 80 μm. Slurry was heated at 70°C for 1 hour using the heating system from the tape caster. Casting was then dried in vacuum oven at 120°C overnight. The casting was then punched into 16 mm circular disc (used as carbon anodes in CR-2016 coin cells)

Isopropanol

The graphite powders were mixed with isopropanol inside a small glass jar (15 mL). Mixing of the powder was done by shaking with hand after sealing the glass jar with a plastic lid. A thin layer (approximately 2 mm) of mixture was then applied on VWR microscope slides by a pipette. The mixture was then left for drying until all the isopropanol has evaporated, leaving a thin layer of graphite powder on the microscope slide. Measurement was done directly on this layer of graphite.

Carbon pellets

Figure 4.1 show the three steps involved in pressing a carbon pellet with a biaxial pressing tool. Powder was first filled into the chosen die with a spatula followed by biaxial compaction. The powder was then ejected from the die. Carbon pellets (ϕ=15 mm) were dry pressed without stearic acid due to the lubricant properties of carbon, the pressure used was 1 ton and pressing time was approximately 5 minutes.

---

[1] C refers to a lithium electrochemical system, R refers to its rounded shape, 2016 refers to a diameter of 20 mm and a height of 1.6 mm respectively [1,2]

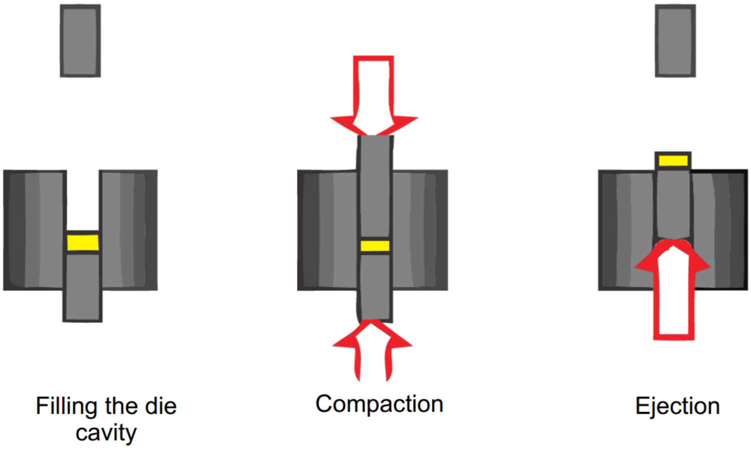

Figure 4.1: The three steps involved in pressing a carbon pellet, the powder shown above is colored yellow for clarity (redrawn from Cunningham et al. [21, p. 3056]

4.1.2 Raman Scattering Measurements

Raman measurements were done on a confocal Horiba Yvon Jobin Labram IR confocal Raman microscope. The instrument was calibrated with a monocrystalline silicon sample before measurements. The laser used was a 633 nm He-Ne laser. The confocal hole for the laser was 100 μm and the filter size was D0.3. The magnitude of the grating was 600. Acquisition time was 60 min with an accumulation number of 4.

The casted and the pellet samples were placed on VWR microscope slides before placing it under the microscope objective for measurements (measurement on the casted samples had the carbon layer facing up). The isopropanol sample was measured directly after sample preparation, with the layer of graphite powder facing up. 36 measurements were done on each sample with a distance of 400 μm between each measuring point on the sample surface. The measuring matrix was thus 6x6 which was chosen to be at the center of the surface sample.

4.1.3 Raman Data Processing

The peak intensities I_D and I_G were acquired by direct reading with Spec Lab 5 Software from Horiba after automatic baseline correction (background removal) with the same software. Integrated peak intensities was obtained by using the built in function in Spec Lab 5 after Lorentz smoothing and fitting of the Raman spectra. The parameters used for baseline correction, smoothing and fitting are summarized in Table 4.2.

Baseline Correction	
Type	Lines
Degree	8

(a)

Smoothing	
Function	Loren()
Level (%)	2
Size (pnt)	100

(b)

Fitting	
Iteration	2
Baseline	Yes

(c)

Table 4.2: The parameters used in Spec Lab 5 for; **(a)** baseline correction, **(b)** smoothing and **(c)** fitting respectively

4.2 X-ray Diffraction Studies

4.2.1 X-ray Sample Preparation

The sample preparation methods are based upon the method established by Iwashita et al. [28] with some slight modifications. Solar grade silicon are used instead of semi conductor grade silicon since what is most important is the crystallinity of the silicon. It is herein assumed that the difference in crystallinity of solar grade silicon compared to semiconductor grade silicon is very small. As a result, it is expected that the results by using solar grade silicon compared to semi conductor grade silicon in the sample preparation method is negligible small. In order to calculate the L_a value, silicon wafer powder was mixed with graphite powder.

The silicon wafer was crushed into a fine powder by an agate mortar before mixing with graphite powder inside a glass holder. Amount of Silicon was approximately 10-15 wt%. The powder was mixed inside a glass holder by adding either isopropanol or ethanol, where the volume ratio of powder: isopropanol, or powder: ethanol was 1:10. Mixing was done by shaking the glass holder for approximately 5 minutes by hand, giving a homogeneous mixture. The mixture was applied on the Si-sample holder by two different methods.

The first method was adding a very thin layer of graphite-isopropanol mixture on the surface of a Si-sample holder by a pipette. The thin layer are smeared out by tilting the Si-sample holder in different direction when the mixture is still wet in order for the mixture to distribute evenly on the Si-sample holder surface. The sample are ready for x-ray diffraction measurements when all the isopropanol from the mixture has evaporated and only a semi-transparent layer of powder are left on the Si-sample holder.

The second method consisted of air spraying a powder-ethanol mixture on the Si-sample holder surface. Air spraying was done with an airbrush obtained from Clas Ohlson store (model AB-119). The air pressure applied was 1.5 bar. The working distance (distance between the Si-sample holder surface and the airbrush nozzle) was approximately 20 cm. Air spraying was done in such a way so that the applied powder was drying almost immediately after the powder-ethanol mixture was applied on the Si-sample holder. Layers of the powder-ethanol mix was applied until a 0.05 mm thick layer of powder was obtained on the sample surface. The silicon surface from the Si-sample holder should not be visible. Isopropanol was used for the first method due to its fluidity, whereas ethanol was used for the second method due to its faster evaporation rate.

4.2.2 X-ray Measurements

A Bruker D-8 Focus X-ray diffractometer without monochromator was used to obtain the X-ray diffraction patterns from the different samples. The metal for generating X-rays from the X-ray tube was Cu, with Kα_1 and Kα_2 wavelengths at 1.54056Åand 1.54439Årespectively. The scanning step size was 0.010 ° and the time spent for each step was 1-3 seconds. Size of the slit was 0.6 mm. and the scanning was done from 77 ° to 79 ° (2θ). The accelerating voltage and the current applied was 40 kV and 40 mA respectively.

4.2.3 X-ray Data Processing

The X-ray diffraction patterns were processed in Bruker AXS Diffrac.Eva version 2 (2011 release) software. Before measuring the FWHM of the Kα_1 from the 311 reflection of silicon and 110 reflection from carbon, Kα_2 stripping was done with the software. Background removal and smoothing of the diffraction pattern were done before measuring the FWHM's with the inbuilt functions from Diffrac.Eva software. Parameters for X-ray data processing are summarized in Table 4.3.

Strip Kα_2	
Max	1
Int. ratio	0.5
Min	1

(a)

Background Removal	
Curvature	1
Threshold	1

(b)

Smoothing	
Max	0.299697
Smooth Factor	0.074
Min	0.009989

(c)

Table 4.3: X-ray parameters for data processing: **(a)** Parameters for stripping of Kα_2 **(b)** Parameters for background removal **(c)** Parameters for smoothing

4.3 SEM Studies

SEM studies were carried out on the three different samples (cast, isopropanol and pellet) for all four graphite powders. The main motivation in using SEM analysis is to characterize morphology, alignment and eventually distinguish edge planes and basal planes visible on the graphite powder surfaces. The graphite samples were analyzed with a FESEM (Field Emission Scanning Electron Microscope) Zeiss Ultra 55 Limited Edition. The applied voltage was 25 kV and the Secondary Electron detector was used for the analysis.

The casted and pellet sample could be analyzed directly when mounted by carbon conductive tabs on the sample holder. However, due to the insulating quality of glass, the isopropanol samples could not be analyzed directly. Instead, new isopropanol samples were prepared directly on the sample holder after sticking a properly sized aluminium sheet on the sample holder by using carbon conductive tabs. The mixtures of isopropanol and graphite were dripped on the aluminium surface with a pipette. The mixtures were left for drying until all the isopropanol had evaporated before SEM analysis. Thickness of the mixtures were approximately 2 mm.

5 Results

5.1 Raman Spectroscopic Results

5.1.1 Raman Spectra

Figure 5.1 shows the Raman spectra for the four different types of graphite powders. All graphite powders exhibits a D band at 1355 [cm^1], a G-band at 1582 [cm^1] and a D′-band at 1622 [cm$^-$1].

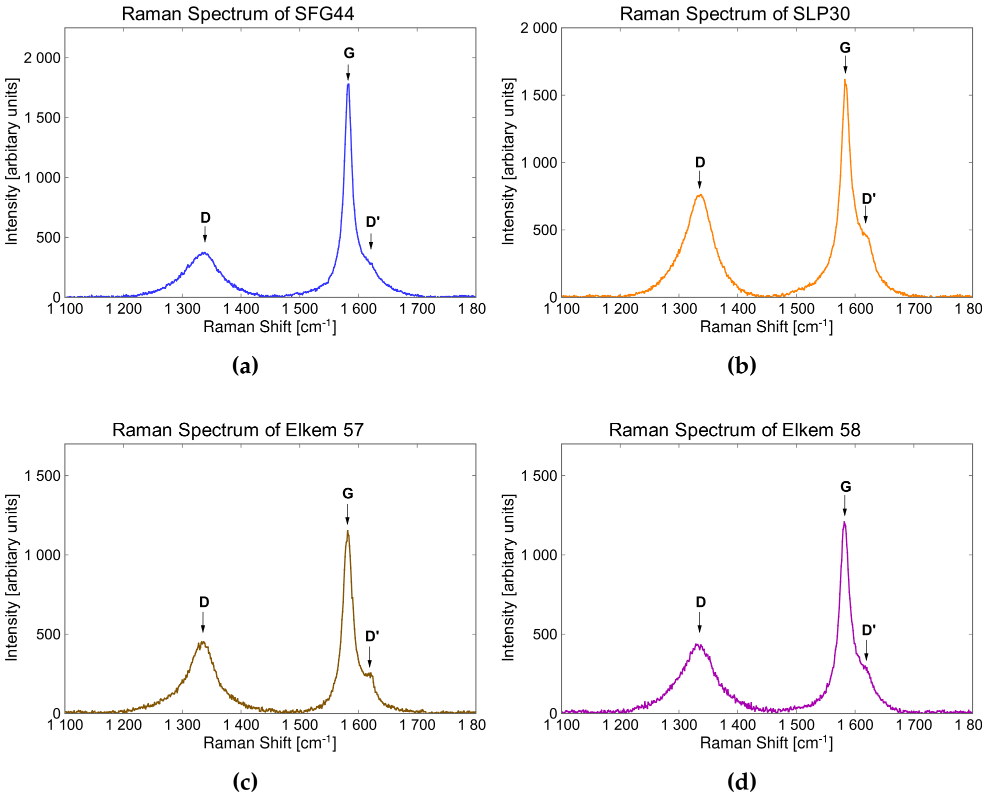

(a) (b) (c) (d)

Figure 5.1: Typical Raman spectra of the four graphite powders: **(a)** SFG44 **(b)** SLP30 **(c)** Elkem 57 **(d)** Elkem 58

5.1.2 R-ratio

The calculated R-ratios of all four graphite powder samples based on the peak height intensity of I_D and I_G are shown in Figures 5.2-5.5. The value of the average R-ratio of SFG44 Cast, Figure 5.2a, is considerable larger than the average R-ratio of SFG44 Isopropanol and SFG44 Pellet samples, Figures 5.2b- 5.2c. This trend is also clearly visible for the SLP30 samples, where the average R-ratio of SLP30 Cast, Figure 5.3a, is much larger than the average R-ratio of SLP30 Isopropanol and SLP30 Pellet, Figure 5.3b-5.3c.

The Elkem samples also show a larger average R-ratio in the samples which are casted, Figure 5.4a, and Figure 5.5a compared to the samples which are prepared with isopropanol, Figure 5.4b and Figure 5.5b. The calculated R-ratios of all four graphite powder samples based on the integrated peak intensity of I_D and I_G are shown in Figures 5.6-5.9. The same trend is visible here as it was with the average R-ratio calculated from peak height intensity. This trend is visible for all four graphite powder samples, where all the casted samples has a larger average R-ratio than the isopropanol and pellet samples respectively.

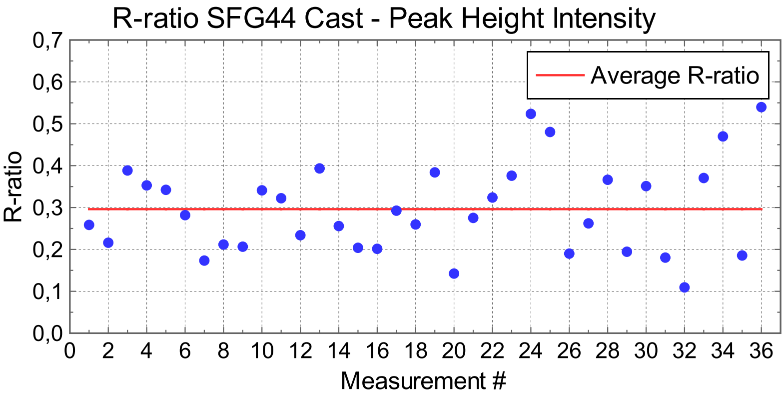

(a)

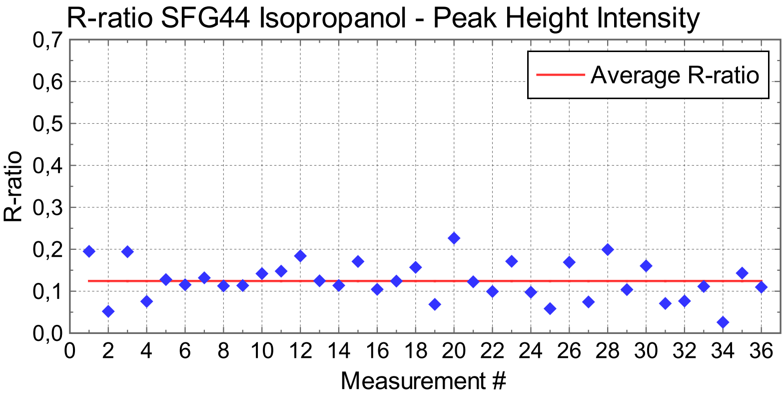

(b)

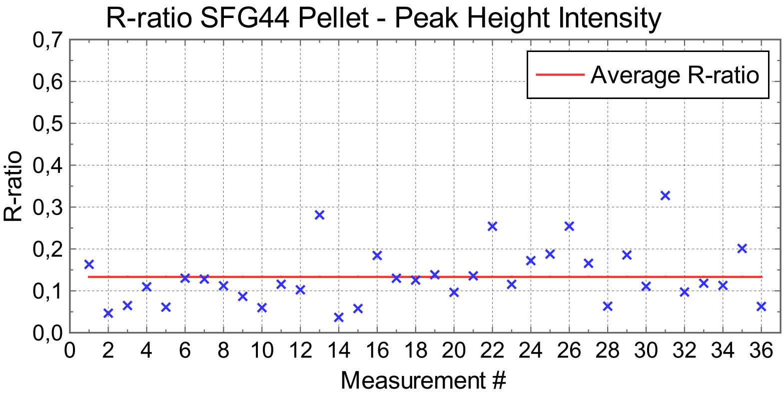

(c)

Figure 5.2: R-ratio of SFG44, calculated from peak height intensity of I_D and I_G: **(a)** R-ratio of all 36 measurements made on SFG44 Cast **(b)** R-ratio of all 36 measurements made on SFG44 Isopropanol **(c)** R-ratio of all 36 measurements made on SFG44 Pellet

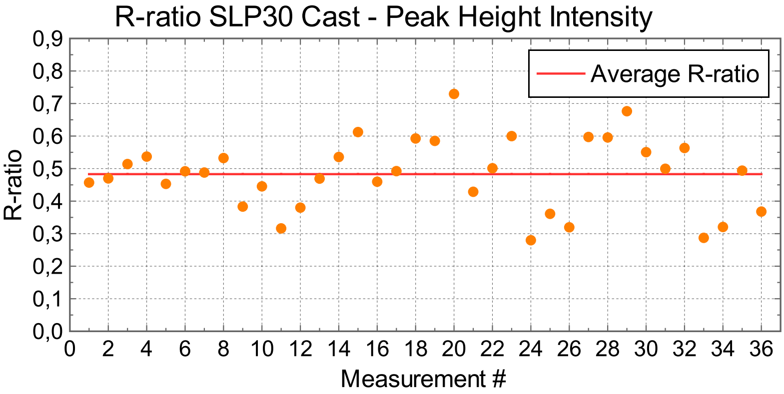

(a)

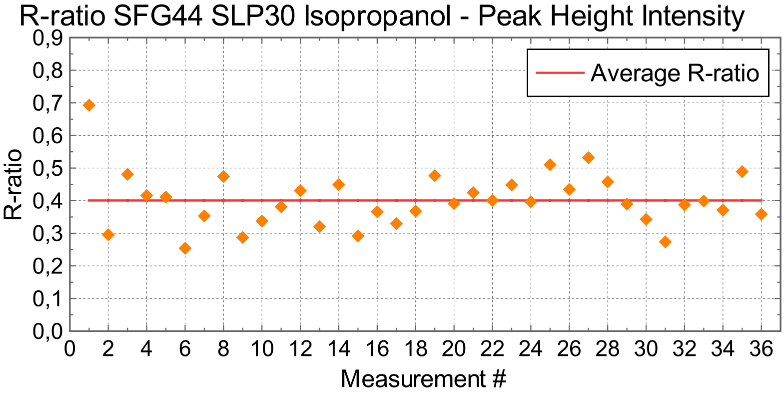

(b)

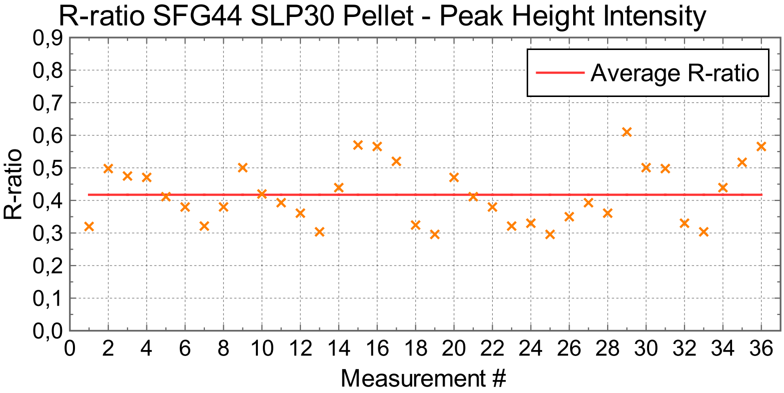

(c)

Figure 5.3: R-ratio of SLP30, calculated from peak height intensity of I_D and I_G: **(a)** R-ratio of all 36 measurements made on SLP30 Cast **(b)** R-ratio of all 36 measurements made on SLP30 Isopropanol **(c)** R-ratio of all 36 measurements made on SLP30 Pellet

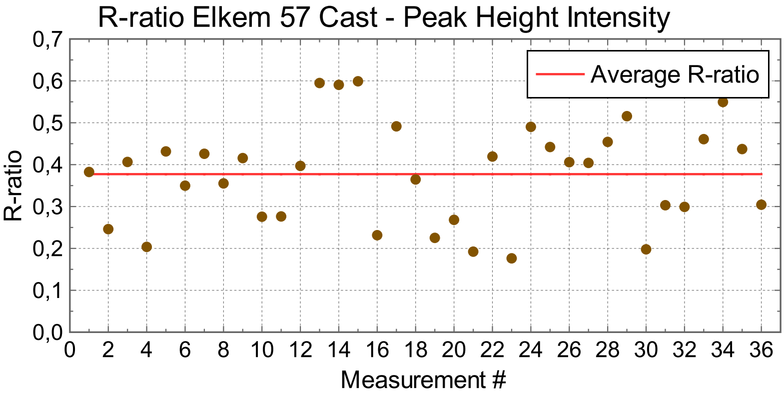

(a)

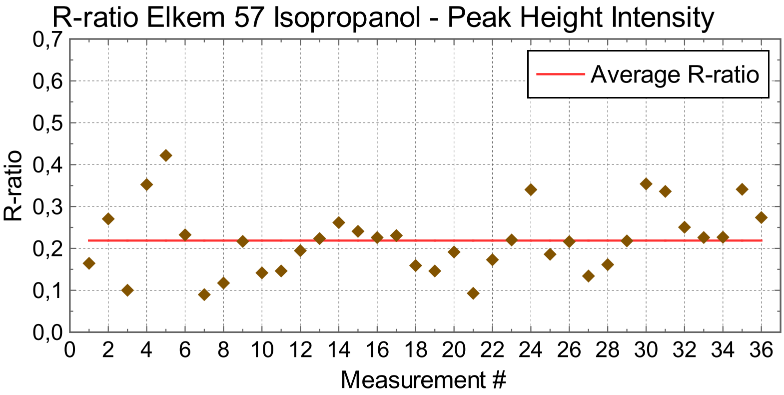

(b)

Figure 5.4: R-ratio of Elkem 57, calculated from peak height intensity of I_D and I_G: **(a)** R-ratio of all 36 measurements made on Elkem 57 Cast **(b)** R-ratio of all 36 measurements made on Elkem 57 Isopropanol

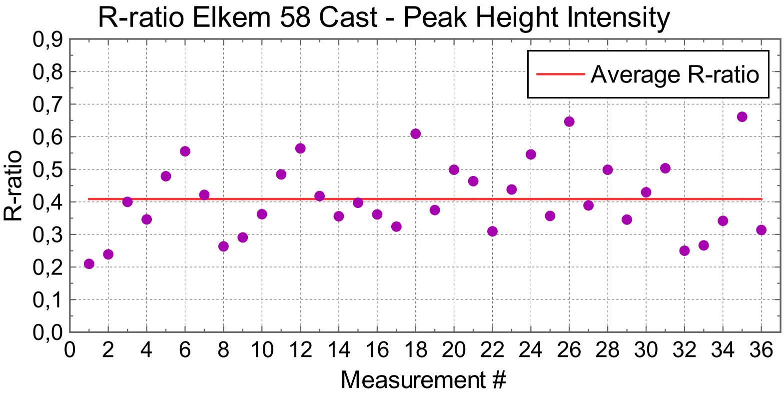

(a)

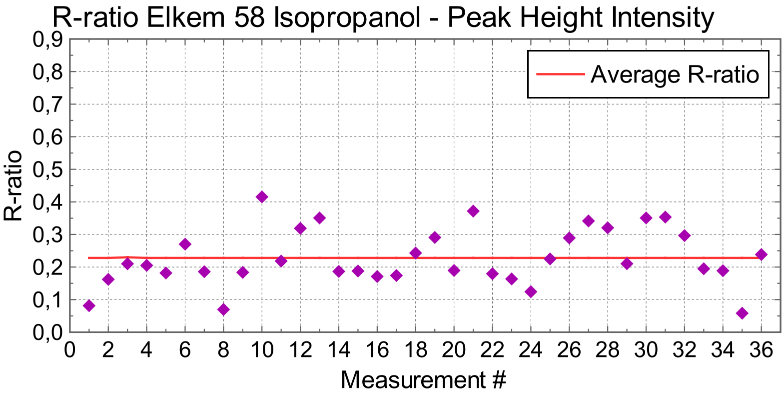

(b)

Figure 5.5: R-ratio of Elkem 58, calculated from peak height intensity of I_D and I_G: **(a)** R-ratio of all 36 measurements made on Elkem 58 Cast **(b)** R-ratio of all 36 measurements made on Elkem 58 Isopropanol

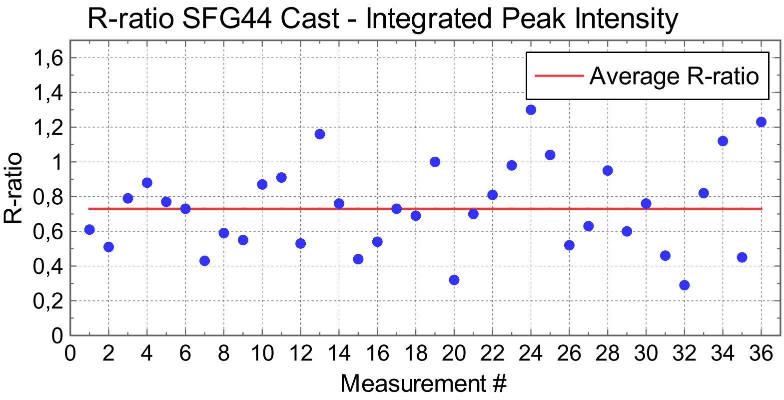

(a)

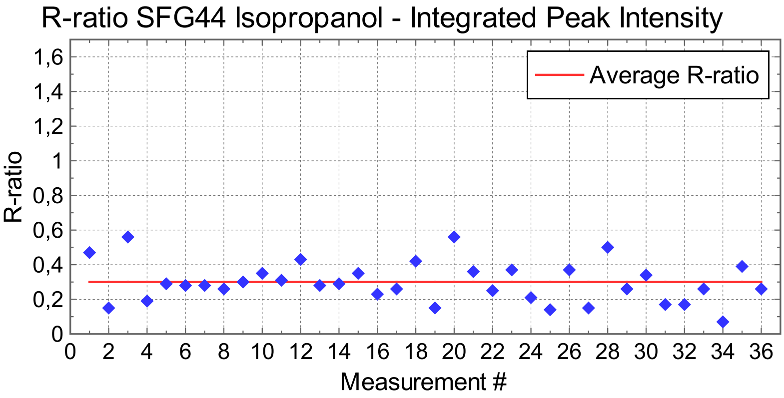

(b)

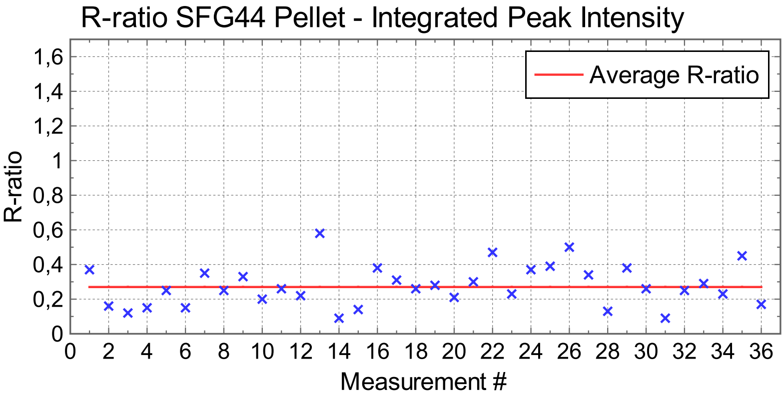

(c)

Figure 5.6: R-ratio of SFG44, calculated from integrated peak intensity of I_D and I_G: **(a)** R-ratio of all 36 measurements made on SFG44 Cast **(b)** R-ratio of all 36 measurements made on SFG44 Isopropanol **(c)** R-ratio of all 36 measurements made on SFG44 Pellet

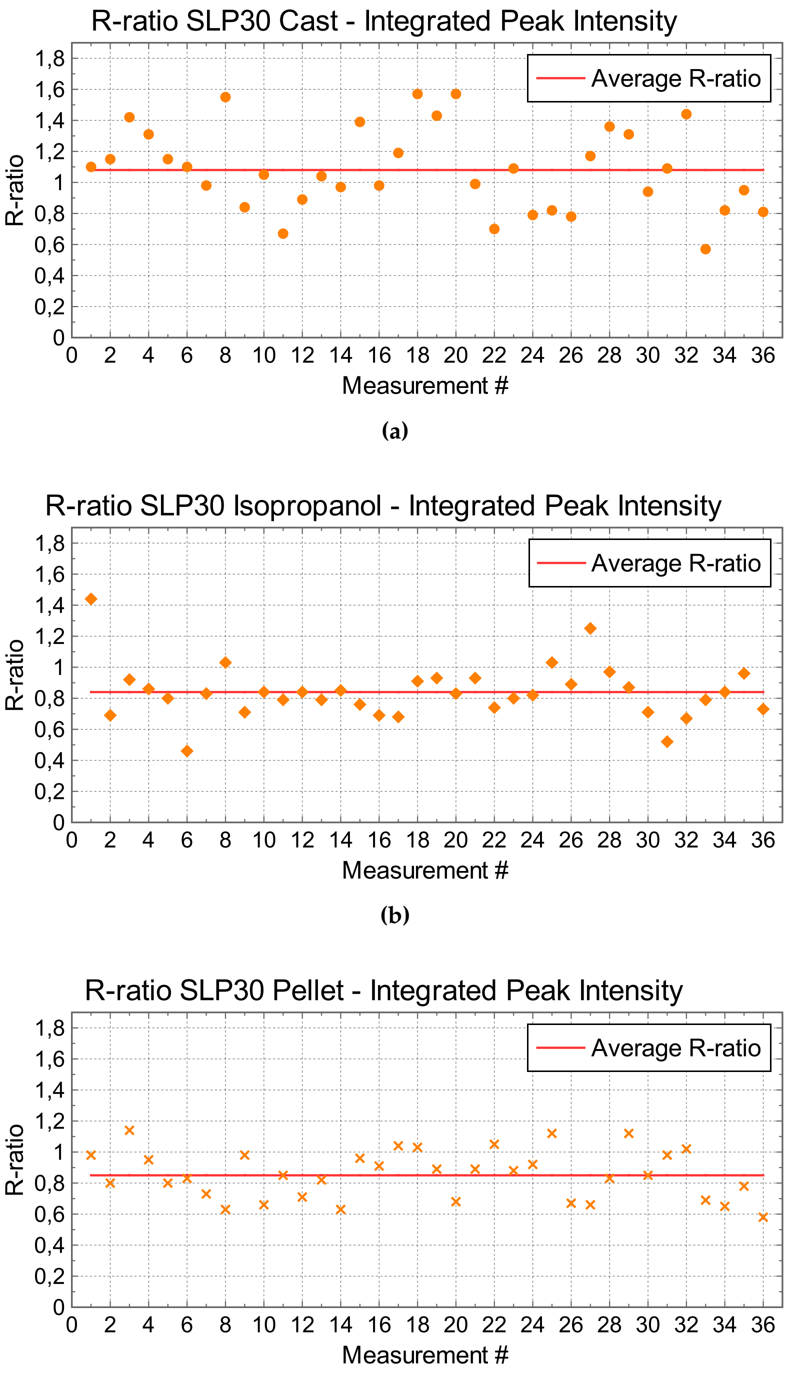

(a)

(b)

(c)

Figure 5.7: R-ratio of SLP30, calculated from integrated peak intensity of I_D and I_G: **(a)** R-ratio of all 36 measurements made on SLP30 Cast **(b)** R-ratio of all 36 measurements made on SLP30 Isopropanol **(c)** R-ratio of all 36 measurements made on SLP30 Pellet

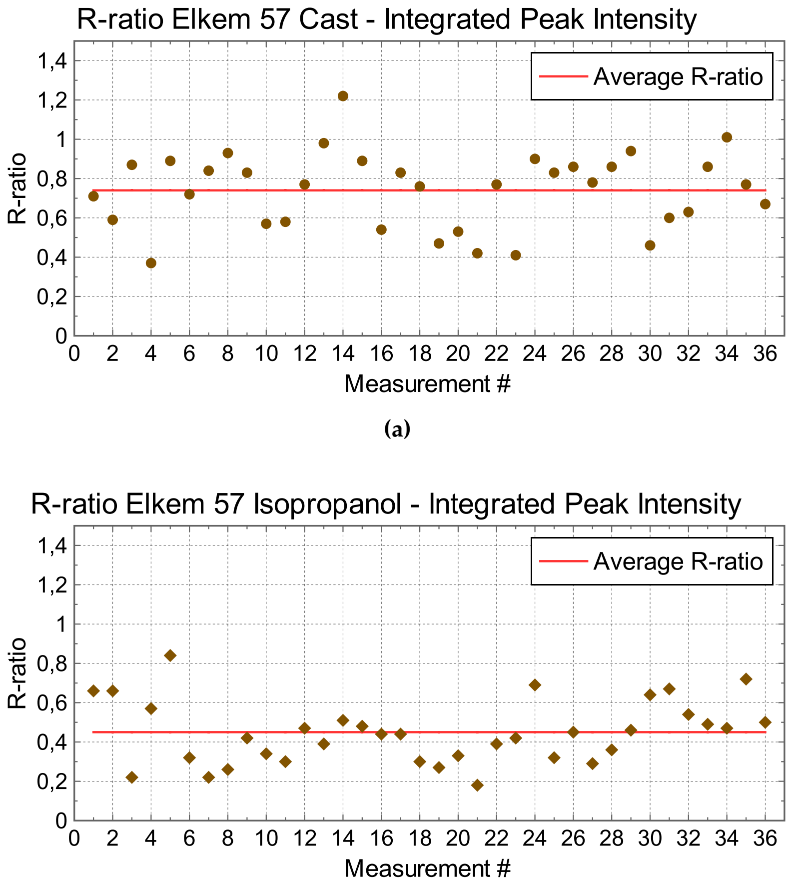

(a)

(b)

Figure 5.8: R-ratio of Elkem 57, calculated from integrated peak intensity of I_D and I_G: **(a)** R-ratio of all 36 measurements made on Elkem 57 Cast **(b)** R-ratio of all 36 measurements made on Elkem 57 Isopropanol

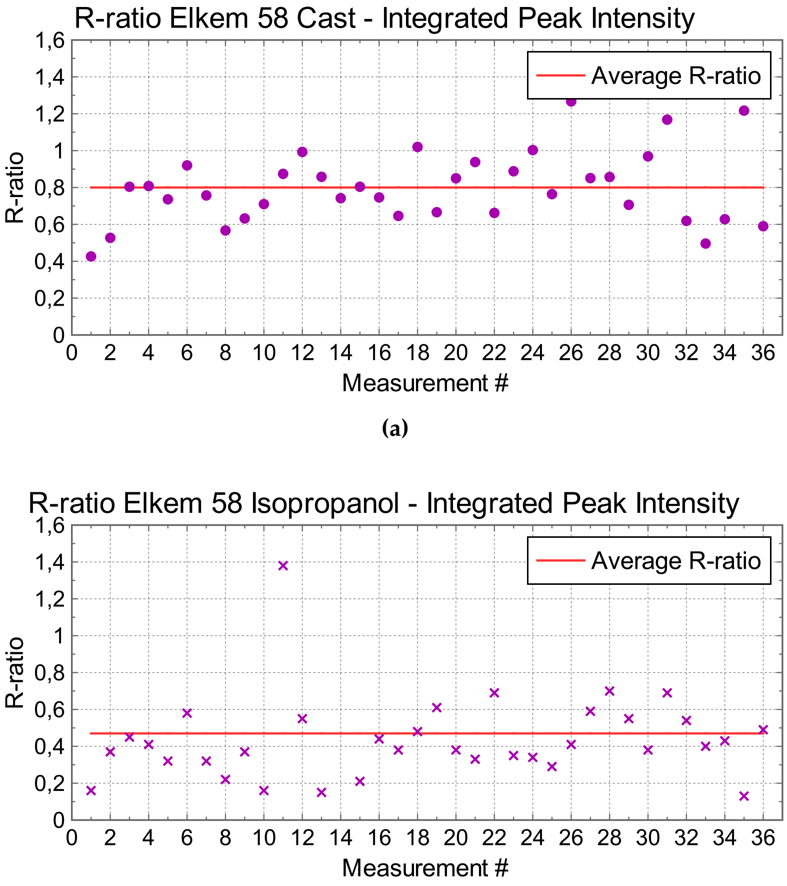

R-ratio Elkem 58 Cast - Integrated Peak Intensity

(a)

R-ratio Elkem 58 Isopropanol - Integrated Peak Intensity

(b)

Figure 5.9: R-ratio of Elkem 58, calculated from integrated peak intensity of I_D and I_G: **(a)** R-ratio of all 36 measurements made on Elkem 58 Cast **(b)** R-ratio of all 36 measurements made on Elkem 58 Isopropanol

Table 5.1 shows a summary of the R-ratio of the graphite powders. All the four types of graphite powders show a higher value of the R-ratio when casted, compared to when the samples are prepared with isopropanol or pressed into pellets, regardless of how the R-ratio was calculated (peak height intensity or integrated peak intensity).

However, SLP30 shows a smaller difference between the casted sample compared to the isopropanol and the pellet sample for both cases. The R-ratio is therefore not independent of the sample preparation method. In addition, the results from the Raman measurements shows no remarkable trend in the value of the standard deviation between the different sample preparation methods

	Peak Height Intensity					
	R-ratio			$\sigma_{R-ratio}$		
Sample	Cast	Iso†	Pellet	Cast	Iso†	Pellet
SFG44	0.296	0.124	0.133	0.107	0.046	0.068
SLP30	0.483	0.401	0.417	0.108	0.085	0.083
Elkem 57	0.380	0.220	N/A*	0.055	0.077	N/A*
Elkem 58	0.410	0.230	N/A*	0.074	0.111	N/A*

(a)

	Integrated Peak Intensity					
	R-ratio			$\sigma_{R-ratio}$		
Sample	Cast	Iso†	Pellet	Cast	Iso†	Pellet
SFG44	0.734	0.295	0.275	0.253	0.117	0.148
SLP30	1.08	0.838	0.853	0.268	0.176	0.151
Elkem 57	0.741	0.446	N/A*	0.194	0.158	N/A*
Elkem 58	0.797	0.472	N/A*	0.195	0.314	N/A*

(b)

Table 5.1: Summary of the average R-ratio from the different types of graphite samples calculated from the **(a)** peak height intensity and from the **(b)** integrated peak height intensity: $\sigma_{R-ratio}$=standard deviation of R-ratio, *carbon pellets could not be formed due to the nature of the graphite powder (the graphite powder did not stick together to form the pellet),†abbreviation for Isopropanol

5.2 SEM Micrographs

Figures 5.10-5.11 show SEM Micrographs of all the different types of samples made from the four graphite powders. Possible damages after the mechanical grinding in the casted samples (Figures 5.10a, 5.10d, 5.11a, 5.11c) is not clearly visible when compared to the isopropanol samples (Figures 5.10b, 5.10e, 5.11b, 5.11d) which looks similar.

The SEM micrographs of SFG44 cast and isopropanol reveal that the graphite particles are flake like. In addition, the graphite particles in SFG44 Cast and SFG44 Isopropanol (Figures 5.10a-5.10b) are more random oriented compared to the graphite particles in SFG44 Pellet (Figure 5.10c). In the SFG44 Pellet sample, the flake like particles has reoriented itself in such a way where the larger areas of the flake like particles is oriented parallel to the sample surface.

The flat potato like morphology of the SLP30 graphite particles is clearly visible in the SEM micrographs of SLP30 cast and isopropanol. In the SLP30 Pellet sample (Figure 5.10f, the graphite particles are also more oriented, showing the same trend as the SFG44 samples. It is clearly visible that the larger areas of the flat potato like morphology are much more parallel to the sample surface compared to the casted sample and the sample prepared with isopropanol.

Elkem samples show a relatively random orientation of the graphite particles of the casted (Figure 5.11a-5.11c) samples and the samples prepared with isopropanol (Figure 5.11b-5.11d). The morphology of the graphite particles of Elkem 57 and Elkem 58 is very similar.

The edge planes of the graphite powders of SLP30 and SFG44 are clearly visible in Figure 5.12. The edge plane on a graphite particle of SFG44 can be seen to be situated at the edge of the flake like particle of SFG44 Figures 5.12a5.12b. The edge plane of the SLP30 particle shown in Figures 5.12c5.12d is also situated at the edge of the flat potato like particle.

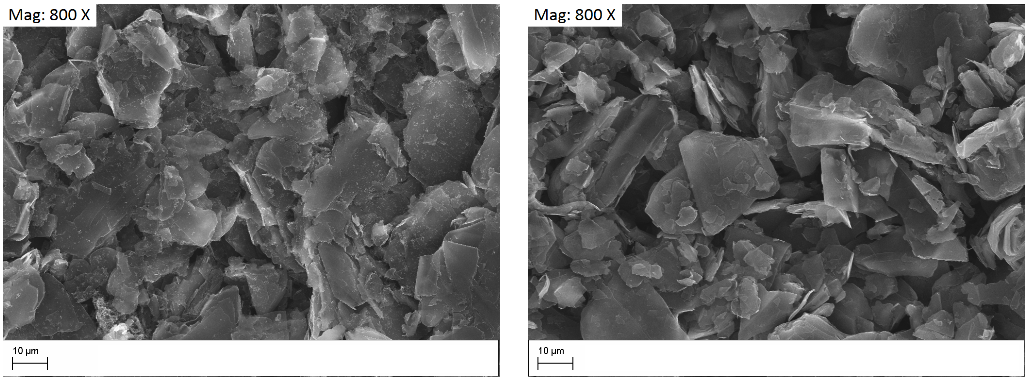

(a) SFG44 Cast

(b) SFG44 Isopropanol

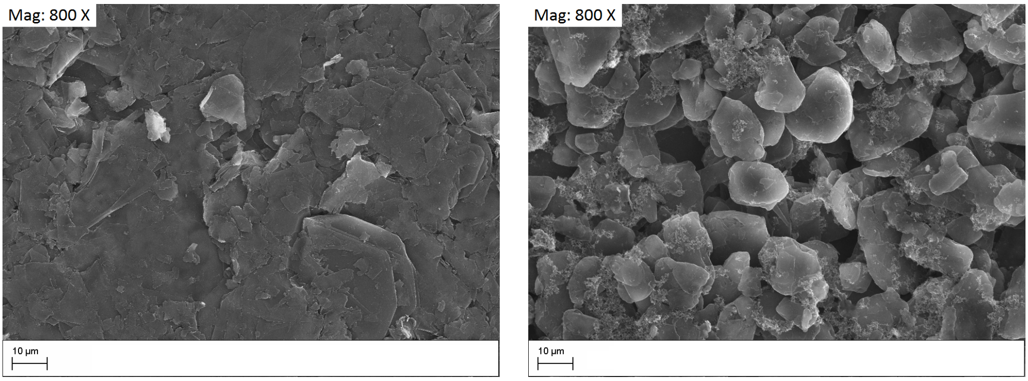

(c) SFG44 Pellet

(d) SLP30 Cast

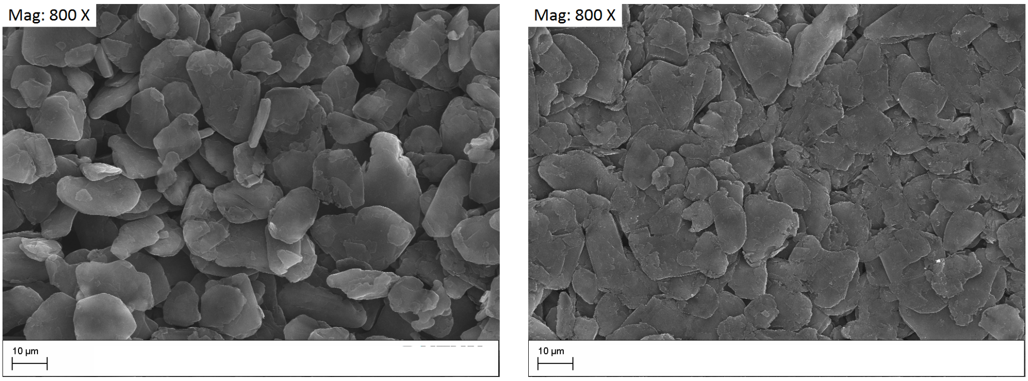

(e) SLP30 Isopropanol

(f) SLP30 Pellet

Figure 5.10: SEM images of SFG44 and SLP30 samples with a magnification at 800x

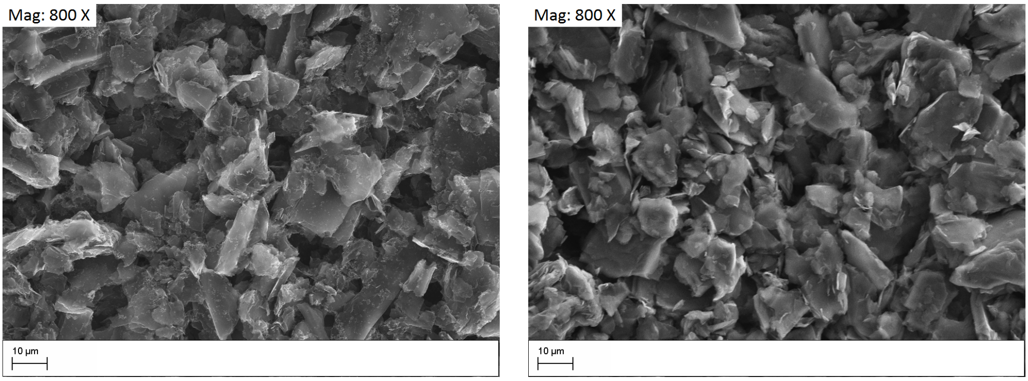

(a) Elkem 57 Cast

(b) Elkem 57 Isopropanol

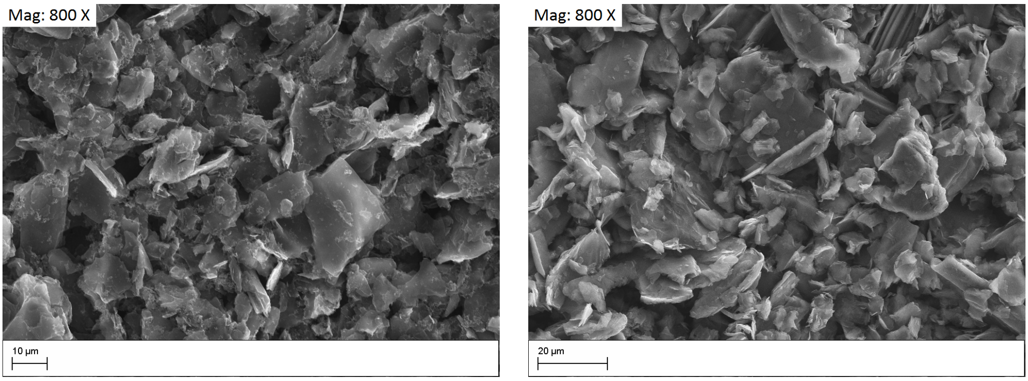

(c) Elkem 58 Cast

(d) Elkem 58 Isopropanol

Figure 5.11: SEM images of Elkem 57 and Elkem 58 samples with a magnification at 800x

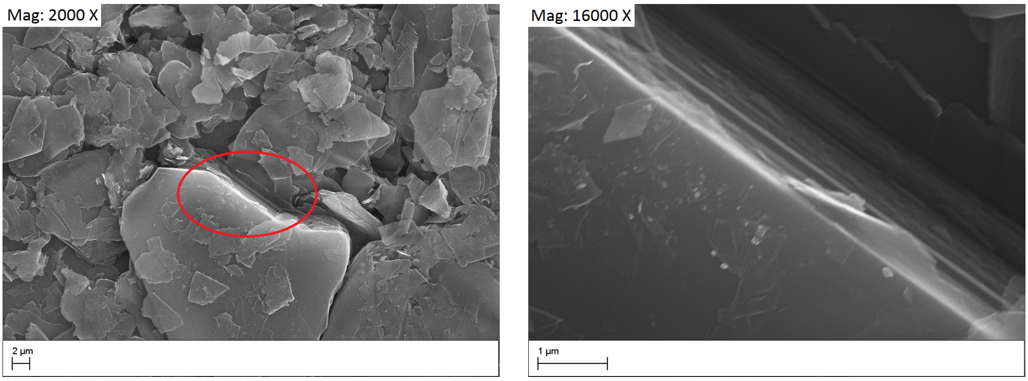

(a) SFG44 Edge Planes at 2000x **(b)** SFG44 Edge Planes at 16000x

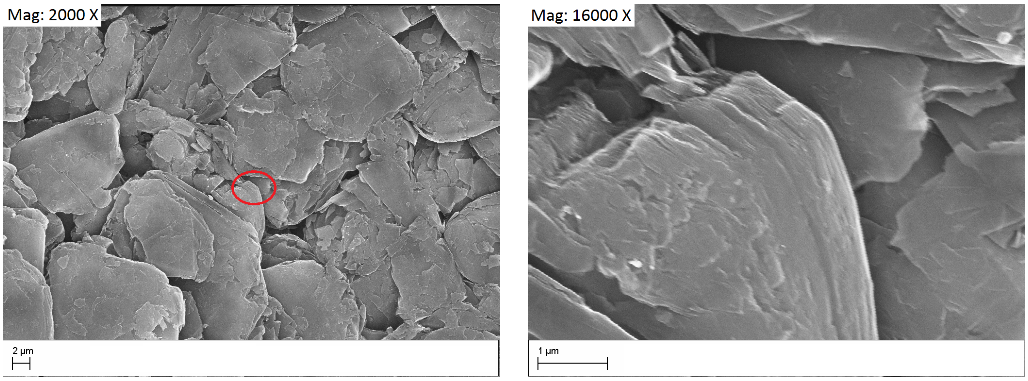

(c) SLP30 Edge Planes at 2000x **(d)** SLP30 Edge Planes at 16000x

Figure 5.12: SEM images of the visible edge planes of a graphite particle in SFG44 Pellet and SLP30 Pellet samples: **(a)** Particle in SFG44 Pellet sample with visible edge planes (marked with a red ellipse) **(b)** Larger magnification of the same particle in SFG44 Pellet showing the edge planes clearly **(c)** Particle in SLP30 Pellet sample with visible edge planes (marked with a red ellipse) **(d)** Larger magnification of the same particle in SLP30 pellet showing the edge planes clearly

5.3 X-ray Diffraction Patterns

Figure 5.13 shows diffraction patterns of Elkem 57 graphite between 77 ° to 78 °.The step size was 0.010 ° with a scanning time of 1 second per step. Figure 5.13a shows the diffraction pattern of the sample preparation in which the mixture has been applied directly on the Si-sample holder.

In Figure 5.13b, the powder has been applied on the Si-sample holder by air spraying.

The diffraction pattern of the air sprayed Elkem 57 sample shows two diffraction peaks from the 110 reflection of carbon (at 77.434 ° and 77.668 °) corresponding to Kα_1 and Kα_2. However, the diffraction pattern obtained from the sample where powder has been applied shows no definite traces of the Kα_1 and Kα_2 peaks. The diffraction patterns of the four silicon-graphite powders between 75 ° to 79 ° (air sprayed) are shown in Figure 5.14 respectively. The wt% of silicon wafer are either 10 or 15 wt%. The amount are chosen according to how "responsive" the graphite powder is. Step size is 0.010 ° with a scanning time of 3 seconds per step. All four powder mixtures show a clear separation of the Kα_1 peak and the Kα_2 peak for both silicon (at 76.305 ° and 76.523 °) and carbon (77.434 ° and 77.668 °).

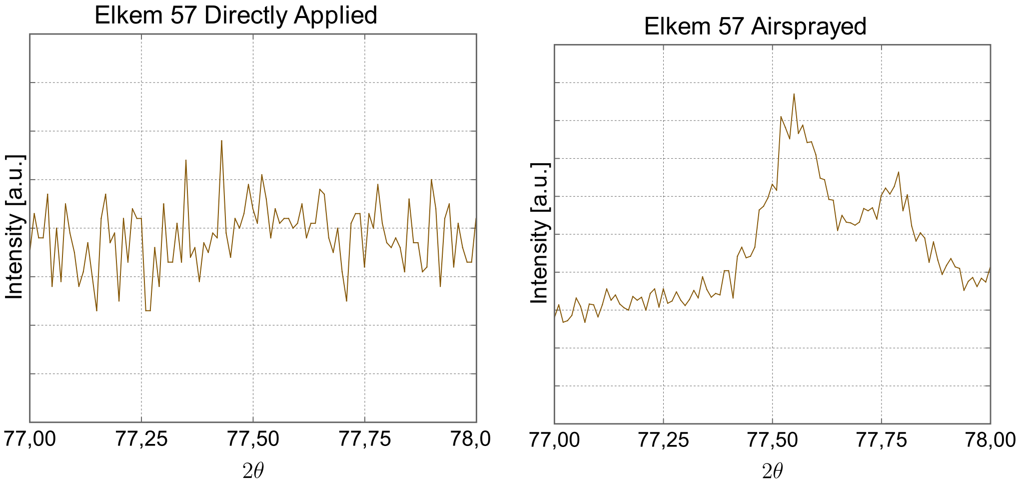

(a)

(b)

Figure 5.13: X-ray diffraction patterns: **(a)** X-ray diffraction pattern of Elkem 57 graphite powder in which the powder has been applied directly on the Si-sample holder **(b)** X-ray diffraction pattern of Elkem 57 graphite in which the powder has been air sprayed on the Si-sample holder

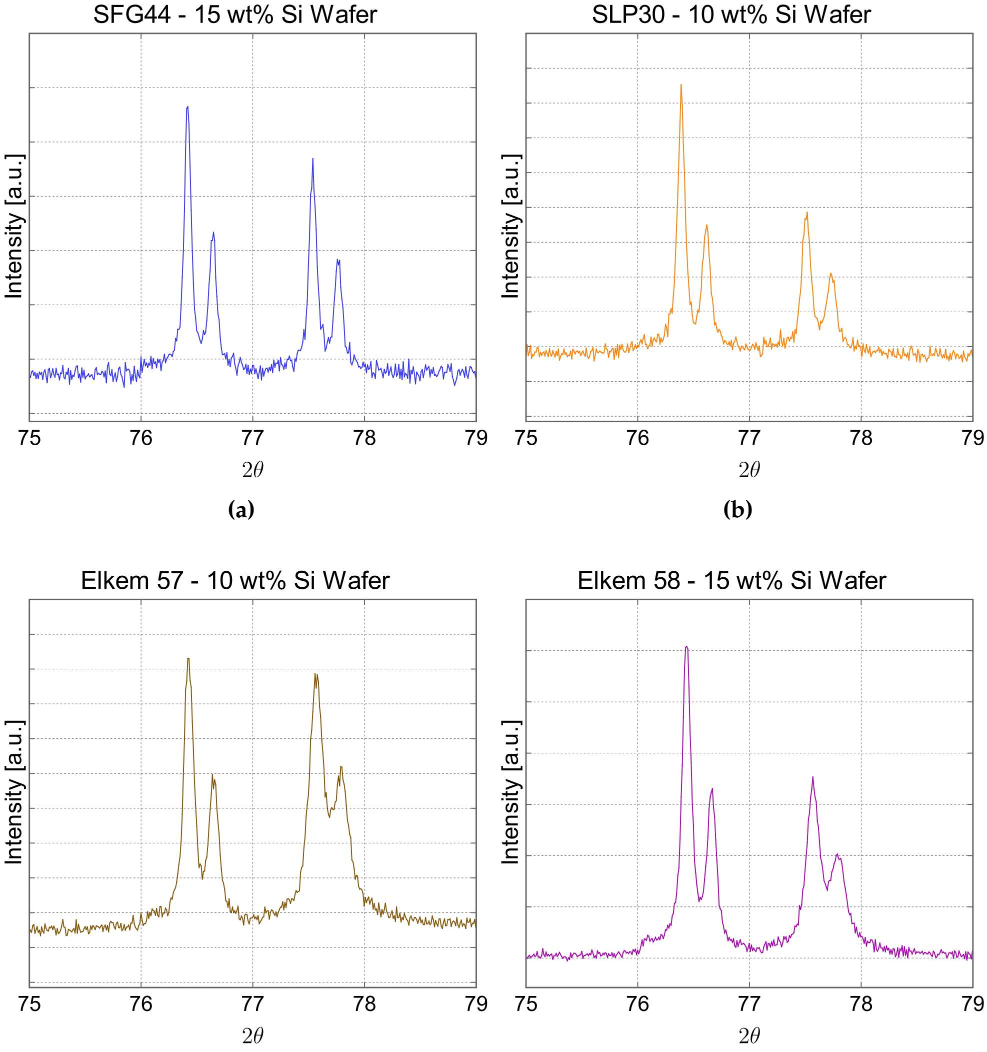

(a) (b) (c) (d)

Figure 5.14: X-ray diffraction patterns of the four different graphite powders which has been air sprayed: **(a)** X-ray diffraction pattern of SFG44 containing 15 wt% silicon wafer **(b)** X-ray diffraction pattern of SLP30 containing 10 wt% silicon wafer **(c)** X-ray diffraction pattern of Elkem 57 containing 10 wt% silicon wafer **(d)** X-ray diffraction pattern of Elkem 58 containing 15 wt% silicon wafer

5.4 Comparison of X-ray- and Raman Studies

A comparison of the calculated L_a values from X-ray diffraction (Equation 3.16) and from Raman measurements (Equation 3.14 are presented in Figure 5.15. The SFG44 and SLP30 samples show a big difference in the L_a value calculated from X-ray diffraction compared to Raman measurements. For the Elkem samples, there is a smaller difference between the L_a value obtained from X-ray measurements compared to Raman measurements.

The size trend is also different for the X-ray measurements compared to Raman measurements. In the X-ray measurements, the L_a value is largest for SFG44 and smallest for Elkem 58 in the following order; SFG44>SLP30>Elkem 57>Elkem 58. The trend for the Raman measurement is different although SFG44 still shows the largest L_a value whereas SLP30 has the smallest R-ratio instead. The size order is SFG44>Elkem 57>Elkem 58>SLP30 for the Raman measurements instead. Of all the L_a values obtained from the Raman measurements, the L_a value obtained from the casted samples have the smallest value for all samples.

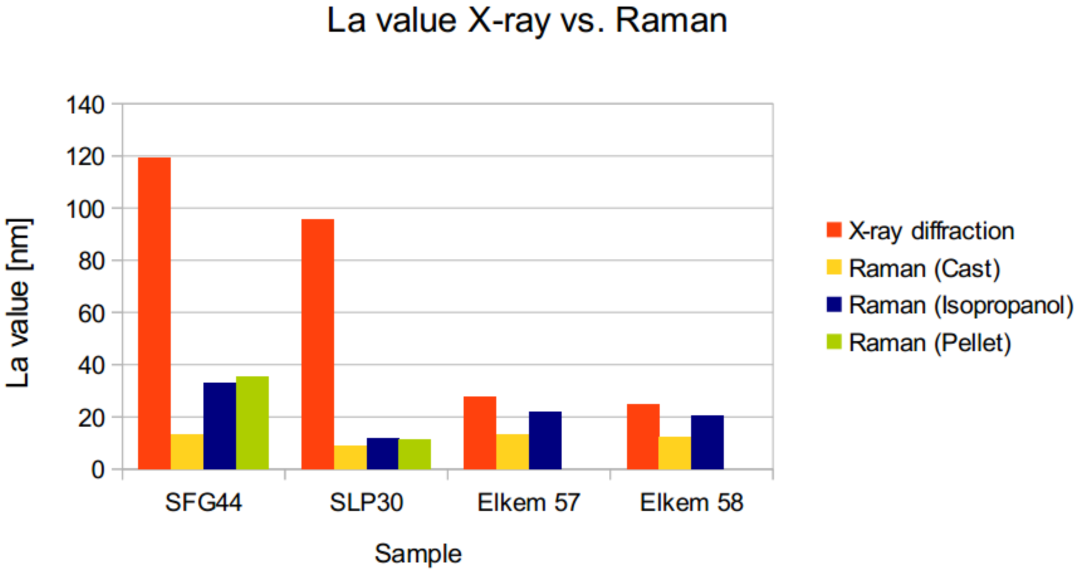

Figure 5.15: A comparison of the L_a value calculated from X-ray diffraction and from the R-ratios obtained from the casted sample, the sample prepared with isopropanol and the pellets respectively. The R-ratio are calculated from the integrated peak intensity of I_D and I_G.

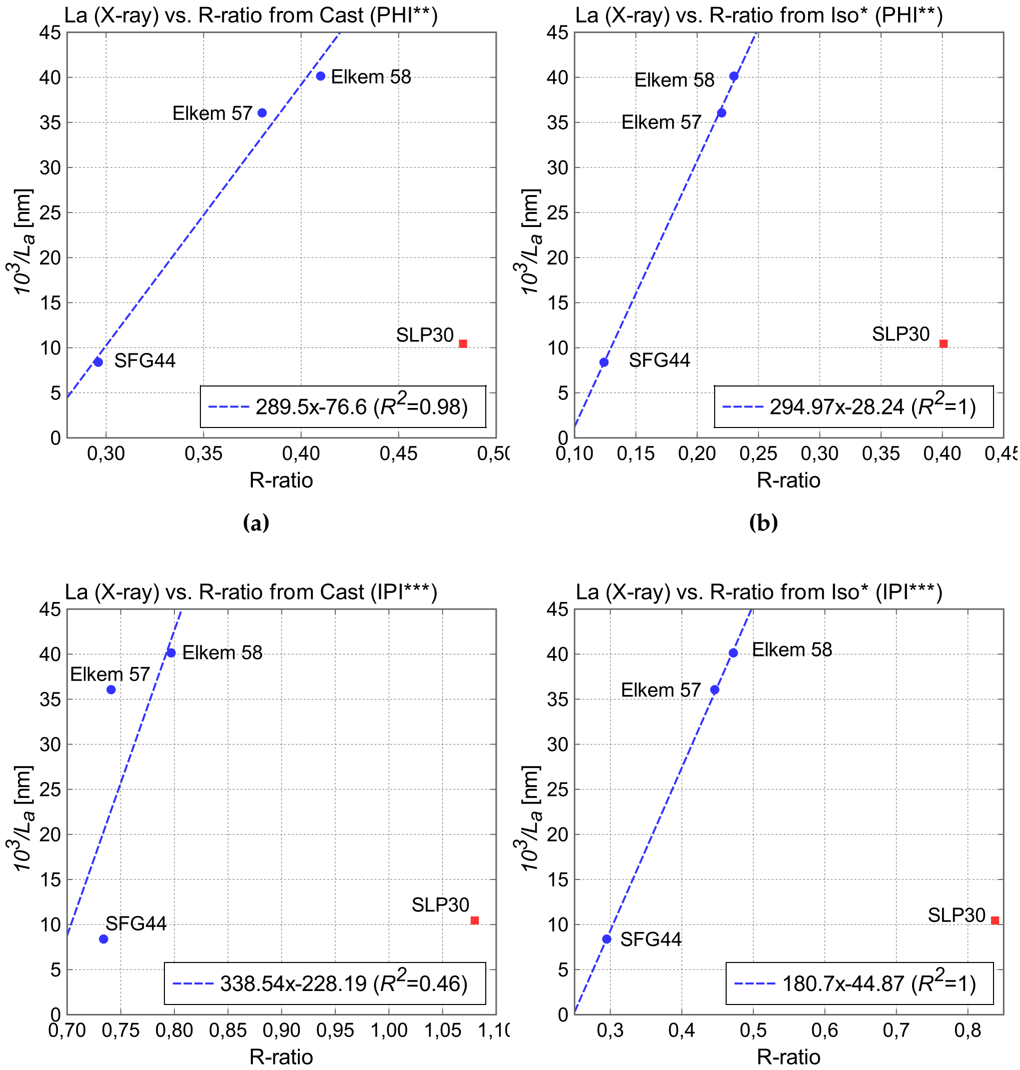

(a) (b) (c) (d)

Figure 5.16: Correlation between the X-ray measured L_a value vs. R-ratio measured from Raman. The blue circular dots represents SFG44, Elkem 57 and Elkem 58 respectively. The red square represents SLP30. The dashed blue line is an equation obtained from linear regression (using least square method) of the positions of SFG44, Elkem 57 and Elkem 58 respectively (*Abbreviation for Isopropanol, **Abbreviation for Peak Height Intensity, ***Abbreviation for Integrated Peak Intensity): **(a)** The L_a value measured from X-ray vs. R-ratio calculated from peak height intensity from casted samples **(b)** The L_a value measured from X-ray vs. R-ratio calculated from peak height intensity from isopropanol samples **(c)** The L_a value measured from X-ray vs. R-ratio calculated from integrated peak intensity from casted samples **(d)** The L_a value measured from X-ray vs. R-ratio calculated from integrated peak intensity from isopropanol samples

Figure 5.16 shows a plot of X-ray measured L_a value vs. Raman R-ratio. Correlation between the X-ray L_a value and the R-ratio are found by linear regression (using least square method) of SFG44, Elkem 57 and Elkem 58 positions, showing a remarkable correlation of the three graphite samples in three out of four cases. This is shown in Figure 5.16a, b and d respectively, in which the coefficient of determination R^2 ranges from 0.98-1[2]. Only the R-ratios which are calculated from the integrated peak intensities from the casted samples of SFG44, Elkem 57 and Elkem 58 show a poor correlation with the X-ray L_a values, Figure 5.16c. The coefficient of determination R^2 is 0.46 for this case, which gives a poor fit of the data.

In all four cases, SLP30 lies far outside this linear relationship which are exhibited by the other three graphite types. Figure 5.17 summarize all the linear regressions which are made in Figure 5.16. Here, it is shown that both the slope and the constant varies for all the linear regressions. The slope ranges approximately from 180 to 338 whereas the constant ranges approximately from 28 to 228.

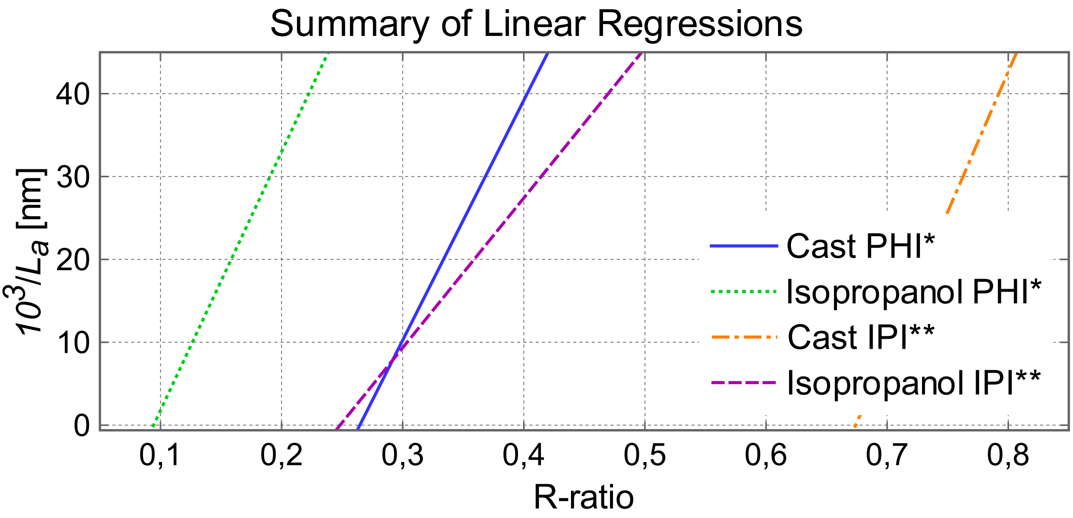

Figure 5.17: Summary of all the linear regressions from Figure 5.16. *Abbreviation for peak height intensity,**abbreviation for integrated peak intensity

---

[2] The coefficient of determination ranges from 0 to 1, where 1 is a good fit and zero means that there is no linear relationship between the dependent and independent variables [10]

The calculated L_a value (Equation 3.16) from the x-ray diffraction patterns (air sprayed samples) are shown in Table 5.2. Table 5.3 summarizes the calculated L_a value by using Equation 3.14.

Sample	L_a value from X-ray [nm]
SFG44	119.1761
SLP30	95.6567
Elkem 57	27.7301
Elkem 58	24.9145

Table 5.2: The calculated L_a value for all graphite types in nanometer from the air sprayed samples[nm]

The L_a value calculated from Raman R-ratio [nm]			
Sample	Cast	Isopropanol	Pellet
SFG44	13.188	32.814	35.200
SLP30	8.963	11.551	11.348
Elkem 57	13.063	21.704	N/A*
Elkem 58	12.146	20.508	N/A*

Table 5.3: Calculated L_a value from the R-ratios obtained from Raman measurements. Calculations are based upon the R-ratio calculated from integrated intensities of the I_D peak and I_G peak

6 Discussion

The repeating trend for all graphite samples is that the casted samples have a higher R-ratio than the samples which was either pressed into pellets or prepared using isopropanol. This can first be rationalized using particle orientation as an argument to this behavior. From the results, it is clearly visible that the particle orientation in the graphite pellets is more aligned in one plane compared to the casted samples. The possible explanation is that since the particle orientation is more random in the casted carbon samples, more edge planes are more exposed on the sample surface of the casted samples compared to the pellet samples (the pellet samples has particle aligned with its basal planes parallel to the particle surface). Since more edge planes is exposed in the casted samples due to the more random particle orientation compared to the pellet samples, a higher R-ratio is expected. This might be the conclusion if the particles in the Isopropanol samples are also more oriented than the casted samples.

However, the SEM micrographs show that the particles in the isopropanol samples have a similar orientation to the casted samples, although the results show that the R-ratio is considerable higher in the casted samples compared to the samples which was prepared with isopropanol. In addition, small difference between the R-ratio of the isopropanol samples (with more random particle orientation) and the R-ratio of the pellet samples (more oriented particle orientation) are observed. Therefore, particle orientation is not the main cause of the higher R-ratio in the casted samples compared to the pellets and the isopropanol samples.

An another possible explanation of the big difference of the R-ratio between the casted samples and the other samples is that the casted samples contain some amount of Carbon Black. If the Carbon Black has a very high R-ratio, it might contribute to a higher R-ratio from the casted samples. This assumption is however less likely due to the very small content of Carbon Black (less than 0.025 wt%). This statement can be confirmed due to that no visible peaks from PVDF at 1433 cm^{-1} [29] in the first order region of graphite is visible although the PVDF content (less than 0.075 wt%) in the carbon cast was larger.

There is however a big difference between the sample preparation between the casted samples compared to the pellet samples and the isopropanol samples. By briefly analyzing the sample preparation methods, the casted sample underwent mechanical grinding in the ball mill for 20 minutes before casting. Although the effect of the ball milling is not clearly visible on the SEM Micrograph, Tommasini et al. has proven that the R-ratio increases with the milling time in his study on nano graphites (see Figure 3.18b) [54]. The trend is that the R-ratio increases much faster when the laser excitation frequency is lower (higher wavelength) between the milling time of 0-100 minutes. It is herein assumed that the four Graphite powders, SFG44, SLP30, Elkem 57 and Elkem 58 are also prone to this milling effect as the nano graphites, which is very likely since the only major difference is the particle size distribution. An another assumption is that since the He-Ne laser wavelength (633 nm) is between 514 nm and 785 nm, the effect on the R-ratio by grinding is something in-between the these two wavelengths. Therefore, a very big increase is observed although the milling time was just 20 minutes (the trend from Tommasizine et al. is that the increase in R-ratio is very drastic for lower wavelengths). It is therefore very likely that the factor which contributes to the larger R-ratio in the casted samples is the ball milling.

The X-ray diffraction patterns which are obtained by applying the powder directly on the Si-sample holder shows no traces of the peaks necessary to calculate the L_a value, Figure 5.13a. It is very likely that this is due to the powder particles, having a particle morphology which are more flake like (instead of spherical). If this is true, then preferred orientation occurs instead of random orientation of the powder particles. The SEM micrograph of Elkem 57 (Figure 5.11b) shows graphite particles which are more flake like than spherical, which confirms the assumption of preferred orientation.

In addition, from the SEM micrographs of all the graphite powders (Figure 5.10b, 5.10e, 5.11b, 5.11d), it is clearly visible that the particles are more flake like (or ellipsoidal for SLP30) than spherical. From the SEM micrographs of SFG44 and SLP30 in Figures 5.12a and 5.12d, the edge planes are clearly visible. Consequently, the flake like powder particles have edge planes situated at the "sharp" edges of the flake like powder particles, whereas the basal planes are situated at the more "flat" like surfaces of the flake like powder particles. It is also assumed that this is the case for the Elkem graphite powders since the morphology of the Elkem graphite powders are similar to the SFG44 particles, although the edge planes could not be resolved by the SEM microscope. When preferred orientation occurs, the 110 planes in graphite which are supposed to "reflect" the X-rays at 77.434° 2θ lies in one preferred orientation instead of being random oriented. As a result, the resolution of the peaks corresponding to the 110 planes are either poor or not even visible from the X-ray diffraction (which are true for this case).

However, when the powder is air sprayed on the Si-sample holder, the powder orientation is a little more random despite the flake like structure of the powder, therefore, clear traces of the $K\alpha_1$ and $K\alpha_2$ from the 110 reflection are visible in the diffraction pattern, Figure 5.13b.

As mentioned in the results, the L_a value which are calculated using Raman measurements compared to X-ray measurements shows huge difference in between them when SFG44 and SLP 30 are investigated, Figure 5.15. However, for Elkem 57 and Elkem 58 graphites, the difference of the L_a value obtained from X-ray and Raman is much less. In fact, the result shows numbers which are no more than approximately ± 6 nm, which is quite remarkable. This result is however derived from the isopropanol samples of Elkem 57 and Elkem 58 from the Raman measurements, Table 5.3 and Table 5.2. The main reason for this surprising trend remains unknown at the moment.

The casted samples of Elkem 57 and Elkem 58 show a larger difference with the X-ray measured L_a value. This is expected since it has already been concluded that the casted samples has an R-ratio which are greatly affected by mechanical grinding. Therefore, it is not surprising that the L_a value calculated from Raman measurements of the casted samples show a value which are even more far off than those obtained from the isopropanol samples (which is true for all four graphite powders).

The L_a value obtained from X-ray measurements show that the Elkem 58 has the smallest crystallite size, whereas in the Raman measurements, the SLP30 has the smallest. To rationalize this behavior, the X-ray diffraction method are compared with the Raman method. As mentioned above, the Raman measurement technique is limited to the surface of the sample which are measured. Changes in the surfaces of the sample might manipulate the outcome of the Raman spectrum, although the bulk of the sample remains the same. In X-ray diffraction, the X-ray penetrates through the whole sample, a more overall "picture" of the structure is therefore expected for the X-ray diffraction method and is not limited to the surface. This would mean that the X-ray diffraction method is more reliable whereas the Raman method is more unreliable. Therefore, the apparently opposing trend between X-ray and Raman might rather be attributed to the more limited Raman spectroscopic technique, which are largely dependent on the structure of the surface of the sample, although the surface structure and bulk structure might be very different.

From Figure 5.16, three out of four cases show a very good correlation between the X-ray measured L_a value and the R-ratio of the three graphite samples SFG44, Elkem 57 and Elkem 58. This good correlation might be attributed to that the morphology of SFG44, Elkem 57 and Elkem 58 is very similar, whereas the morphology of SLP30 is ellipsoidal. If surface structures/defects are dependent on the morphology of the graphite powder, then the inverse proportional empirical relationship between the R-ratio and the X-ray measured L_a value might differ from the case of Tuinstra et al. (Equation 3.12. The findings of Nikiel et al. on their work of nuclear graphites strengthen this assumption [42]. Therefore, the deviation from the linearity is very likely attributed to the SLP30 morphology compared to the SFG44, Elkem 57 and Elkem 58 morphology.

The linear regressions shown in Figure 5.17 gives an indicative of the unreliability of using Raman spectroscopy to determine the R-ratio. Here, it is shown that both the slope and the constant of the linear regression lines vary a lot. The R-ratio has been shown to be dependent on the sample preparation method, the particle morphology and the surface induced defected by mechanical grinding earlier. Also shown in the Figure is that it is unreliable to depend on the relationship of Tuinstra et al., since the magnitude of the variations of the slope and the constants of the linear regressions lines might be large enough to differ from the equations which are derived from the empirical Tuinstra et al. relationship. Doing calculations by using Equation 3.12 or Equation 3.14 to get the L_a value might therefore give large errors. As a result, using

Raman spectroscopy alone to calculate the L_a value is unreliable.

However, if Raman measurements are supported with X-ray measurements, a relationship of the X-ray measured L_a value and the R-ratio can be derived specifically for a graphite type of powder. The Tuinstra et al. relationship cannot be relied on alone. Restriction has to be put on the graphite powder such as morphology, sample preparation, surface induced defects from mechanical stress, etc. This fact is weakly proven by the linear relationship exhibited by SFG44, Elkem 57 and Elkem 58 in Figure 5.16.

7 Conclusion

It is established that the R-ratio is largely dependent on the sample preparation of the graphite powder prior to Raman measurements. When mechanical grinding are done on the graphite powders, the measured R-ratio increases compared to when the graphite powders are measured directly without undergoing some mechanical grinding of some sort.

Air spraying of graphite powders has been established as a method to increase the resolution of the diffraction peaks for obtaining the L_a value. This is due to the air sprayed powder particles being more randomly oriented when being air sprayed on the Si-sample holder surface. Air spraying can therefore be used as a method to counteract preferred orientation when the powder particles are more flake like than spherical.

Using Raman spectroscopy alone to determine the crystallite size L_a in the basal plane of graphite powder is unreliable since several factors affects the R-ratio. These variables are mechanical stress on the graphite powder, sample preparation, and particle morphology might also affect the R-ratio greatly. Therefore, using Raman spectroscopy to determine the L_a value of graphite can only be reliable when complementary X-ray diffraction has been utilized. Restrictions has to be put on the graphite powder due to the factors affecting the R-ratio mentioned before.

8 Further Work

Due to time constraints and unexpected complexity of the Raman R-ratio, investigations on how the L_a value affects the critical parameters of a carbon anode could not be performed. Therefore, a natural suggestions to further work is to investigate the correlation between the L_a value and the cycling performance of a carbon anode.

It has already been shown that the R-ratio has a correlation with the rate capability of a carbon anode from earlier work [46]. Furthermore, Belenkov has shown that the interatomic distances in the graphene sheets and the interplanar spacing d_{002} between the basal planes of graphite depends on the crystallite size L_a [14]. It can be deduced that structural disordering can occur due to expansion of the graphite structure due to the Li-ion occupying the available sites between the graphene sheets. Also, if the interatomic distance between the atoms in the graphene sheets is unusually small, the capacity might also be affected. The findings of Belenkov might therefore be interesting in further studies of the L_a value versus capacity of graphite.

9 Acknowledgments

I would like to thank Associate Professor Fride Vullum-Bruer (NTNU), Research Scientist Anita Fossdal (SINTEF), Research Scientist Edel Sheridan (SINTEF), scholarship holder Carl Erik Lie Foss (NTNU) and Bartlomiej Gawel (NTNU) for their help in various topics and laboratory routines. Special thanks to Chief Engineer Julian R. Tolchard who came up with the idea of air spraying graphite powders on Si-sample holder for the X-ray characterization part.

References

[1] Battery nomenclature. `http://en.wikipedia.org/wiki/Battery_nomenclature`. [Online; accessed 05-February-2012].

[2] Button cell. `http://en.wikipedia.org/wiki/Button_cell`. [Online; accessed 05-February-2012].

[3] Electron diffraction and crystal structure. `http://instructor.physics.lsa.umich.edu/adv-labs/Electron_Diffraction/electron_diffraction2.pdf`. [Online; accessed 06-January-2012].

[4] Graphite in lubrication fundamental parameters and synergism with mos2. `http://www.timcal.com/scopi/group/timcal/timcal.nsf/pagesref/SCMM-7FGFCP/$File/Leaflet_Graphite_in_Lubrication_Fundamental_Parameters_and_Synergism_with_MoS2.pdf`. [Online; accessed 10-October-2011].

[5] Introduction to raman spectroscopy. `http://www.perkinelmer.com/CMSResources/Images/44-74565MAN_Raman20Questions.pdf`. [Online; accessed 5-October-2011].

[6] Killacycle specs. and the killacycle team. `http://www.killacycle.com/about/`. [Online; accessed 2-February-2012].

[7] Mobile energy - li-ion batteries. `http://www.timcal.com/scopi/group/timcal/timcal.nsf/pagesref/SCMM-7EVDST?OpenDocument&Lang=en`. [Online; accessed 5-February-2012].

[8] Nanophosphate basics: An overview of the structure, properties and benefits of a123 systems proprietary lithium ion battery technology. `http://info.a123systems.com/white-paper-nanophosphate-lithium-ion-battery`. [Online; accessed 2-February-2012].

[9] Raman scattering. `http://www.doitpoms.ac.uk/tlplib/raman/raman_scattering.php?printable=1`. [Online; accessed 30-September-2011].

[10] Statistics. `http://www.britannica.com/EBchecked/topic/564172/statistics/60716/Analysis-of-variance-and-goodness-of-fit?anchor=ref367496`. [Online; accessed 25-January-2012].

[11] X-ray tube. `http://www.britannica.com/EBchecked/topic/650502/X-ray-tube`. [Online; accessed 9-January-2012].

[12] R. Baddour-Hadjean and J. P.Pereira-Ramos. Raman microspectrometry applied to the study of electrode materials for lithium batteries. *Chemical Reviews*, 110:1278–1319, 2010.

[13] M. R. Baldan, E. C. Almeida, A. F. Azevedo, E. S. Gonçalves, M. C. Rezende, and N. G. Ferreira. Raman validity for crystallite size la determination on reticulated vitreous carbon with different graphitization index. *Applied Surface Science*, 254:600–603, 2007.

[14] E. A. Belenkov. Formation of graphite structure in carbon crystallites. *Inorganic Materials*, 37:928–934, 2001.

[15] I. Buchmann. What is the c-rate? `http://batteryuniversity.com/learn/article/what_is_the_c_rate`. [Online; accessed 1-December-2012].

[16] L. G. Cançado, A. Jorio, E. H. M. Ferreira, F. Stavale, C. A. Achete, R. B. Capaz, M. V. O. Moutinho, A. Lombardo, T. S. Kulmala, and A. C. Ferrari. Quantifying defects in graphene via raman spectroscopy at different excitation energies. *Nano Letters*, 11:3190–3196, 2011.

[17] M. F. Charlier, A. Charlier, and D. Fristot. Binary graphite intercalation compounds. *Journal of Physics and Chemistry of Solids*, 50:987–996, 1989.

[18] D. D. L. Chung. Review graphite. *Journal of Materials Science*, 37:1475–1489, 2002.

[19] G. Compagnini, O. Puglisi, and G. Foti. Raman spectra of virgin and damaged graphite edge planes. *Carbon*, 35:1793–1797, 1997.

[20] A. Cuesta, P. Dhamelincourt, J. Laureyns, A. Martínez-Alonso, and J. M. D. Tascón. Comparative performance of x-ray diffraction and raman microprobe techniques for the study of carbon materials. *Journal of Materials Chemistry*, 8:2875–2879, 1998.

[21] N. Cunningham, M. Lefèvre, J. Dodelet, Y. Thomas, and S. Pelletier. Structural and mechanical characterization of as-compacted powder mixtures of graphite and phenolic resin. *Carbon*, 43:3054–3066, 2005.

[22] R. S. Das and Y. K. Agrawal. Raman spectroscopy: Recent advancements, techniques and applications. *Vibrational Spectroscopy*, 57:163–176, 2011.

[23] D. Doerffel and S. A. Sharkh. A critical review of using the peukert equation for determining the remaining capacity of lead-acid and lithium-ion batteries. *Journal of Power Sources*, 155:395–400, 2006.

[24] J. R. Ferraro, K. Nakamoto, and C. W. Brown. *Introductory Raman Spectroscopy*. Academic Press, 2003.

[25] D. Goers, H. Buqa, L. Hardwick, A. Würsig, and P. Novák. Raman spectroscopic and structural studies of heat-treated graphites for lithium-ion batteries. *Ionics*, 9:258–265, 2003.

[26] T. Gruber, T. W. Zerda, and M. Gerspacher. Raman studies of heat-treated carbon blacks. *Carbon*, 32:1377–1382, 1994.

[27] Y. Huang and R. J. Young. Effect of fibre microstructure upon the modulus of pan- and pitch-based carbon fibres. *Carbon*, 33:97–107, 1995.

[28] N. Iwashita, C. R. Park, H. Fujimoto, M. Shiraishi, and M. Inagaki. Specification for a standard procedure of x-ray diffraction measurements on carbon materials. *Carbon*, 42:701–714, 2004.

[29] Y. Ji, J. Liu, Y. Jiang, and Y. Liu. Analysis of raman and infrared spectra of poly (vinlydine fluoride) irradiated by krf excimer laser. *Spectrochimicta Acta Part A*, 70:297–300, 2008.

[30] S. P. Jones, C. C. Fain, and D. D. Edie. Structural development in mesophase pitch based carbon fibers produced from naphthalen. *Carbon*, 35:1533–1543, 1997.

[31] R. Joyce. Sony recalls pc batteries. `http://www.reuters.com/article/2008/10/31/us-sony-battery-idUSTRE49U1EZ20081031?feedType=RSS&feedName=technologyNews`, 2008. [Online; accessed 20-January-2012].

[32] G. Katagiri, H. Ishida, and A. Ishitani. Raman spectra of graphite edge planes. *Carbon*, 26:565–571, 1988.

[33] D. S. Knight and W. B. White. Characterization of diamond films by raman spectroscopy. *Journal of Materials Research*, 4:385–393, 1989.

[34] R. Kurzweil and K. Brandt. Secondary batteries - lithium rechargeable systems. *Encyclopedia of Electrochemical Power Sources*, pages 1–26, 2009.

[35] D. Kushnir and B. A. Sanden. Multi-level energy analysis of emerging technologies: a case study in new materials for lithium ion batteries. *Journal of Clean Production*, 19:1405–1416, 2011.

[36] P. Larkin. *Infrared and Raman Spectroscopy*. Elsevier Inc., 2011.

[37] M. J. Matthews, M. A. Pimenta, G. Dresselhaus, M. S. Dresselhaus, and M. Endo. Origin of dispersive effects of the raman d band in carbon materials. *Physical Review B*, 59:6585–6588, 1999.

[38] T. P. Mernagh, R. P. Cooney, and R. A. Johnson. Raman spectra of graphon carbon black. *Carbon*, 22:39–42, 1984.

[39] F. A. Miller and G. B. Kauffman. C. v. raman and the discovery of the raman effect. *Journal of Chemical Education*, 66:795–801, 1989.

[40] G. A. Nazri and G. Pistoia, editors. *Lithium Batteries - Science and Technology*. Springer, 2009.

[41] S. H. Ng, C. Vix-Guterl, P. Bernardo, N. Tran, J. Ufheil, H. Buqa, J. Dentzer, R. Gadiou, M. E. Spahr, D. Goers, and P. Novák. Correlations between surface properties of graphite and the first cycle specific charge loss in lithium-ion batteries. *Carbon*, 47:705–712, 2009.

[42] L. Nikiel and P. W. Jagodzinski. Raman spectroscopic characterization of graphites: A re-evaluation of spectra/structure correlation. *Carbon*, 31:1313–1317, 1993.

[43] M. A. Pimenta, G. Dresselhaus, M. S. Dresselhaus, L. G. Cançado, A. Jorio, and R. Saito. Studying disorder in graphite-based systems by raman spectroscopy. *Physical Chemistry Chemical Physics*, 9:1276–1291, 2007.

[44] S. Reich and C. Thomsen. Raman spectroscopy of graphite. *Philosophical Transactions of the Royal Society A*, 362:2271–2288, 2004.

[45] D. N. Sathyanarayana. *Vibrational Spectroscopy: Theory And Applications*. New Age International, 2007.

[46] H. Sato, N. Sato, H. Asahina, S. Yamaguchi, and S. Mori. Raman spectra and rate capability of graphite anode for lithium ion battery. *Denki Kagaku*, 66:1253–1259, 1998.

[47] B. Scrosati and J. Garche. Lithium batteries: Status, prospects and future. *Journal of Power Sources*, 195:2419–2430, 2009.

[48] E. Smith and G. Dent. *Modern Raman Spectroscopy - A Practical Approach*. John Wiley and Sons, Ltd, 2005.

[49] R. Spotnitz. Simulation of capacity fadenext term in lithium-ion batteries. *Journal of Power Sources*, 113:72–80, 2002.

[50] F. C. Tai, C. Wei, S. H. Chang, and W. S. Chen. Raman and x-ray diffraction analysis on unburned carbon powder refined from fly ash. *Journal of Raman Spectroscopy*, 41:933–937, 2010.

[51] P. Tan, S. Dimovski, and Y. Gogotsi. Raman scattering of non-planar graphite: arched edges, polyhedral crystals, whiskers and cones. *Philosophical Transactions of the Royal Society of London A*, 362:2289–2310, 2004.

[52] J. M. Tarascon and M. Armand. Issues and challenges facing rechargeable lithium batteries. *Nature*, 414:359–367, 2001.

[53] C. Thomsen and S. Reich. Double resonant scattering in graphite. *Physical Reviews Letters*, 84:5214–5217, 2000.

[54] M. Tommasini, C. Castiglioni, G. Zerbi, A. Barbon, and M. Brustolon. A join raman and epr spectroscopic study on ball-milled nanographites. *Chemical Physics Letters*, 516:220–224, 2011.

[55] F. Tuinstra and J. L. Koenig. Raman spectrum of graphite. *The Journal of Chemical Physics*, 53:1126–1130, 1970.

[56] A. Tullo. Dell recalls lithium batteries. `http://pubs.acs.org/cen/news/84/i34/8434notw4.html`, 2006. [Online; accessed 20-January-2012].

[57] P. Verma, P. Marie, and P. Novák. A review of the features and analyses of the solid electrolyte interphase in li-ion batteries. *Electrochimica Acta*, 55:6332–6341, 2010.

[58] R. P. Vidano and D. B. Fischbach. Observation of raman band shifting with excitation wavelength for carbons and graphites. *Solid State Communications*, 39:341–344, 1981.

[59] J. M. Walter. Raman spectroscopy of graphite. `http://www.jumwalter.de/raman.htm`. [Online; accessed 17-October-2011].

[60] Y. Wang, D. C. Alsmeyer, and R. L. McCreery. Raman spectroscopy of carbon materials: Structural basis of observed spectra. *Chemistry of Materials*, 2:557–563, 1990.

[61] A. R. West. *Basic Solid State Chemistry*. John Wiley and Sons Ltd, 1999.

[62] C. Yuqin, L. Hong, W. Lie, and L. Tianhong. Irreversible capacity loss of graphite electrode in lithium-ion batteries. *Journal of Power Sources*, 68:187–190, 1997.

[63] G. A. Zickler, B. Smarsly, N. Gierlinger, H. Peterlik, and O. Paris. A reconsideration of the relationship between the crystallite size l_a of carbons determined by x-ray diffraction and raman spectroscopy. *Carbon*, 44:3239–3246, 2006.